JJ-2101

Design of a Fixed Wing Micro Aerial Vehicle

A Major Qualifying Project Report
Submitted to the Faculty of the
WORCESTER POLYTECHNIC INSTITUTE
in Partial Fulfillment of the Requirements for the
Degree of Bachelor of Science
in Aerospace Engineering

by

Ty Bugdin

Sophia Henehan

Noah Shoer

Matthew Shriner

John Trainor

Dieter Teirlinck

Stephen Weaver

April 6, 2021

Approved by:

Jagannath Jayachandran, Advisor
Asst. Professor, Aerospace
Engineering Dept. WPI

David Olinger, Co-Advisor
Assoc. Professor, Aerospace
Engineering Dept. WPI

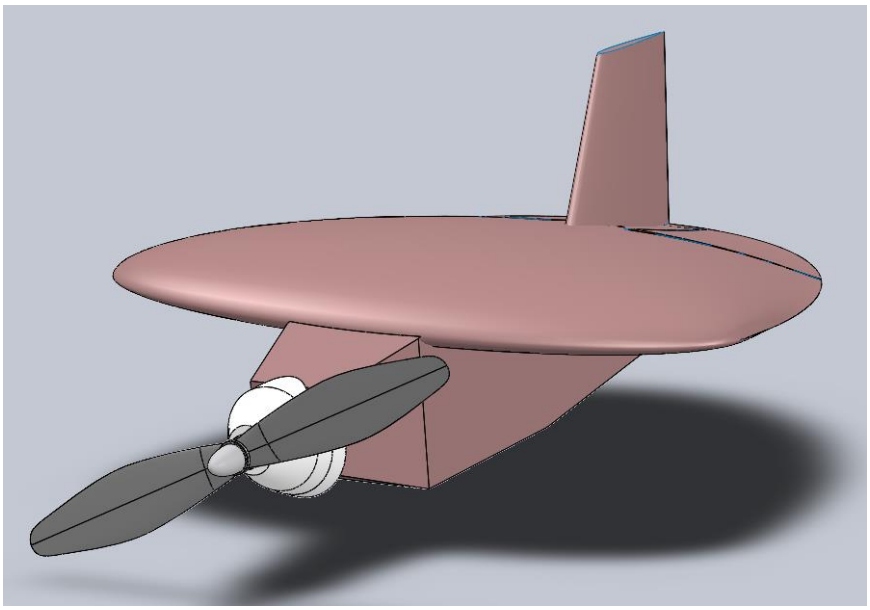

Completed MAV Design

ABSTRACT

The goal of this project was to design, build, and fly a Micro Aerial Vehicle (MAV) to compete in the WPI MAV Competition. Points were awarded based on the aircraft's largest dimension, flight time, ability to carry a payload, and perform onboard inertial measurements. Research was geared to design the smallest MAV while ensuring a four-minute flight time. An iterative design process was undertaken to arrive at the final MAV: a high-wing, fixed vertical tail aircraft, utilizing a Zimmerman wing planform with an area of 734 cm^2 and a Selig 2027 airfoil, constructed out of polystyrene foam. The mass of the MAV was approximately 492 g. The MAV was powered by a lithium-polymer battery and Park 370 brushless motor and controlled by two elevons through a standard 2.4 GHz radio.

ACKNOWLEDGMENTS

The 2021 Micro Aerial Vehicle MQP team would like to thank Professor Jagannath Jayachandran, the team's advisor, and Professor David Olinger, the team's co-advisor, for their exceptional professional assistance throughout the project. We would also like to thank Mrs. Tina Stratis, the secretary for the Aerospace Engineering Department, for assistance in ordering the necessary materials for this project. Finally, we would like to thank our pilot, Jack Tulloch.

TABLE OF AUTHORSHIP

SECTION	**AUTHOR**
1 Introduction	SJW
1.1 Background and Lit. Review	SEH/TFB
1.1.1 Aerodynamics	JTT/NTS/DT
1.1.2 Structures	SEH/MDS
1.1.3 Stability	SJW/NTS
1.1.4 Controls	SJW
1.1.5 Propulsion	NTS/TFB/DT
1.1.6 Reviewed MAVs	SJW/SEH
1.2 Project Goals	TFB/SEH
1.3 Project Design Requirements…	TFB/SEH
1.4 Project Management	SJW
1.5 MQP Objectives…	SEH
1.6 MQP Tasks and Timetable	SEH
1.7 Specifications and Design Summary	NTS/SHE/DT
2 Preliminary Design and Analysis	JTT
2.1 Airfoils	JTT/DT
2.2 Planforms	JTT
2.3 Conceptual Fuselage Designs	NTS
2.4 Stability	JTT
2.4.1 Static Stability	SJW/JTT/SEH

2.4.2 Dynamic Stability	SJW/JTT
3 Detailed Design and Analysis	SEH
3.1 Aerodynamics	JTT
3.1.1 Airfoil	JTT
3.1.2 Planform	NTS
3.1.3 CFD Modeling	JTT
3.1.4 Wind Tunnel Testing	JTT
3.2 Fuselage	MDS/NTS
3.3 Control	SJW
3.3.1 Control Surfaces	NTS
3.3.2 Flight Controller	SJW/JTT/SEH
3.4 Electronics	NTS
3.5 Propulsion	NTS
3.5.1 Static Thrust	NTS/SEH/DT
3.5.2 Dynamic Thrust	DT/TFB
4 Final Design Modifications	MDS
4.1 Fuselage	MDS
4.2 Wing	MDS/SEH
4.3 Control Surfaces	MDS
4.4 Electronics	NTS
5 Fabrication and Construction	SEH
5.1 Initial Steps	MDS/TFB
5.1.1 Tools and Materials	MDS

5.1.2 Lab Procedures and Safety	MDS/DT
5.2 Fabrication	MDS
5.2.1 Wing	MDS
5.2.2 Fuselage	SEH
5.2.3 Control Surfaces	SEH
6 Flight Test Analysis	SEH
6.1 Lasso Test	SJW/DT/SEH
6.2 Glide Tests	SJW/SEH
6.3 Powered Flight Test	SJW/SEH
7 Competition Review	MDS
8 Summary, Conclusions…	MDS/TFB/NTS
8.1 Recommendations for Future Work	MDS/NTS
8.2 Project Broader Impacts	MDS/TFB

TABLE OF CONTENTS

ABSTRACT ..... *i*

ACKNOWLEDGMENTS ..... *ii*

TABLE OF AUTHORSHIP ..... *iii*

TABLE OF CONTENTS ..... *vi*

LIST OF FIGURES ..... *viii*

LIST OF TABLES ..... *x*

NOMENCLATURE ..... *xi*

1 INTRODUCTION *13*

1.1 Background and Literature Review **13**

1.1.1 Aerodynamics 14

1.1.2 Structures 17

1.1.3 Stability 19

1.1.4 Controls 21

1.1.5 Propulsion 23

1.1.6 Reviewed MAVs 24

1.2 Project Goals **26**

1.3 Project Design Requirements, Constraints, and Other Considerations **27**

1.4 Project Management **29**

1.5 MQP Objectives, Methods, and Standards **30**

1.6 MQP Tasks and Timetable **31**

1.7 Specifications and Design Summary **32**

2 PRELIMINARY DESIGN AND ANALYSIS *35*

2.1 Airfoils **35**

2.2 Planforms **41**

2.3 Conceptual Fuselage Designs **43**

2.4 Stability **45**

2.4.1 Static Stability 45

2.4.2 Dynamic Stability 46

3 DETAILED DESIGN AND ANALYSIS *55*

3.1 Aerodynamics **55**

3.1.1 Airfoil 55

3.1.2 Planform 56

3.1.3 CFD Modeling 56

3.1.4 Wind Tunnel Testing 61

3.2 Fuselage **63**

3.3 Control **68**

3.3.1 Control Surfaces 68

3.3.2 Flight Controller 69

3.4 Electronics **70**
3.5 Propulsion **72**
3.5.1 Static Thrust 73
3.5.2 Dynamic Thrust 75
4 FINAL DESIGN MODIFICATIONS ***77***
4.1 Fuselage **77**
4.2 Wing **78**
4.3 Control Surfaces **79**
4.4 Electronics **80**
5 FABRICATION AND CONSTRUCTION ***81***
5.1 Initial Steps **81**
5.1.1 Tools and Material 81
5.1.2 Lab procedures and safety 83
5.2 Fabrication **84**
5.2.1 Wing 84
5.2.2 Fuselage 87
5.2.3 Control Surfaces 90
6 TESTING AND ANALYSIS ***92***
6.1 Lasso Tests **92**
6.2 Glide Tests **93**
6.3 Powered Flight Test **94**
7 COMPETITION REVIEW ***95***
8 SUMMARY, CONCLUSIONS, RECOMMENDATIONS, BROADER IMPACTS ***96***
8.1 Recommendations for Future Work **96**
8.2 Project Broader Impacts **97**
9 REFERENCES ***98***
10 APPENDICES ***102***
Appendix 1: E-Flite Model Power Requirements **102**
Appendix 2: WPI Internal Competition Rules **103**
Appendix 3: WPI MAV Virtual Competition Rules **111**
Appendix 4: Airfoil Performance Scores **114**

LIST OF FIGURES

Figure 1. Laminar Separation Visualization (Winslow, 2018).....16
Figure 2. Typical MAV Foams (Eubanks, 2018). 17
Figure 3. Various foam densities (kg/m^3) plotted for mechanical strength by flexural and compressive strength (kPa). Data source: (Corning, 2011).....18
Figure 4. Airfield Layout.....27
Figure 5. Score vs. Max Linear Dimension.....28
Figure 6: Gantt Chart of Project Schedule 31
Figure 7. Final MAV Design Drawing.....33
Figure 8. CAD Model of Final MAV Design.....34
Figure 9: Completed MAV.....34
Figure 10. Maximum Lift-to-Drag Ratio vs. Aspect Ratio 37
Figure 11. (a) Cruising Velocity & (b) Wing Loading vs. MAV Mass for different wingspans ..38
Figure 12. XFOIL Airfoil Discretization (Drela, 1989).....39
Figure 13. Selig 2046 Lift Curve 41
Figure 14. (a) Zimmerman Wingtip Refinement & (b) Full Wing 43
Figure 15. Initial Fuselage Conceptual Design.....43
Figure 16. Second Fuselage Conceptual Design 44
Figure 17. Modified Wing for Fuselage.....44
Figure 18. Conceptual Wing and Fuselage.....44
Figure 19. Static Margin vs. Aspect Ratio 46
Figure 20. Short Period vs. Phugoid Motion.....47
Figure 21. Dutch Roll Mode.....51
Figure 22. s2027 Airfoil 55
Figure 23. CFD Domain Schematic.....58
Figure 24. Lift Force Fluctuations 59
Figure 25. (a) Lift & (b) Drag Coefficient vs. Angle of Attack 60
Figure 26. Wind Tunnel Lift Curve 62
Figure 27. Lift Coefficient vs. Angle of Attack.....63
Figure 28. Detailed Fuselage Design 64
Figure 29. Inside of Fuselage 65
Figure 30. Nose Cone Front and Back 66
Figure 31. Assembled Nose Cone.....66
Figure 32. Fuselage Without Nose Cone.....67
Figure 33. Fuselage Design with Nose Cone 67
Figure 34. Control Surface Push Rod 69
Figure 35. Deflected Control Surfaces.....69
Figure 36. Static Thrust Testing Diagram 73
Figure 37. Annotated Static Thrust Testing Setup.....74
Figure 38. Motor Testing Setup.....75
Figure 39. Dynamic Thrust as a Function of Velocity.....76
Figure 40. Final Fuselage Iteration 78
Figure 41. Wing and Wing with 27.5% Increased Wingspan 79
Figure 42. Control Rods Inserted in Elevon.....80
Figure 43. Cutting the Basic Pieces 84

Figure 44. Aligning Spars and Foam 85
Figure 45. Glue Curing Setup....85
Figure 46. Foam Cutting the Wing Shape....86
Figure 47. The Sanded Wing....86
Figure 48. Final Wing Before Sanding. 87
Figure 49. Assembled Final Wing. 87
Figure 50. Fuselage Balsa Guides....88
Figure 51. Foam fuselage. 88
Figure 52. Foam wing with 3D printed nose cone.....89
Figure 53. Final Fuselage Side-View....90
Figure 54. Supporting Control Rod....91
Figure 55. Still from Lasso Test 92
Figure 56. Still from Glide Test....93
Figure 57. Still from Powered Flight Test....94

LIST OF TABLES

Table 1. Aircraft Wing Shapes 14
Table 2. Control Surface Area Percentages....21
Table 3. Design Summary of Reviewed MAVs 25
Table 4. Subgroup Members and Responsibilities 29
Table 5: Design Specifications 32
Table 6: Weight Buildup List 32
Table 7. Longitudinal Stability Modes for s2046 (XFLR5)....49
Table 8. Longitudinal Stability Modes for s2027 (XFLR5)....49
Table 9. Longitudinal Stability Modes for Eppler 328 (XFLR5) 50
Table 10. Lateral Stability Modes for s2046 (XFLR5)....52
Table 11. Lateral Stability Modes for s2027 (XFLR5)....52
Table 12. Lateral Stability Modes for Eppler 328 (XFLR5) 53
Table 13. Longitudinal Stability Modes for s2046 with Vertical Stabilizer (XFLR5) 54
Table 14. Lateral Stability Modes for s2046 with Vertical Stabilizer (XFLR5) 54
Table 15. s2027 Aerodynamic Data....56
Table 16. Planform Characteristics....56
Table 17. Electronic Components Considered 71
Table 18. Motor and ESC Specifications 71
Table 19: Electronic Options for Differing MAV Sizing 72

NOMENCLATURE

AC	=	Aerodynamic Center
AR	=	Aspect Ratio
A_n	=	Number of Inertial Measurements
b	=	Wingspan
c	=	Chord
CAD	=	Computer-Aided Design
C_d	=	Drag Coefficient Per Unit Span
C_l	=	Lift Coefficient Per Unit Span
C_m	=	Moment Coefficient Per Unit Span
C_D	=	Drag Coefficient
C_L	=	Lift Coefficient
C_M	=	Moment Coefficient
CG	=	Center of Gravity
D	=	Drag
DC	=	Direct Current
e	=	Oswald Efficiency Factor
ESC	=	Electronic Speed Controller
GPS	=	Global Positioning System
h	=	Location of Center of Gravity
Im	=	Imaginary Component
K	=	Induced Drag Factor
k_n	=	Static Margin
L	=	Lift
LiPo	=	Lithuim-ion Polymer (battery)
LSB	=	Laminar Separation Bubble
l_V	=	Tail Arm
MAC	=	Mean Aerodynamic Chord
MAV	=	Micro Air Vehicle
PWM	=	Pulse-width Modulation
Re	=	Reynolds Number, Real Component

S, S_W = Wing Surface Area

S_V = Tail Area

t = Time

u_∞ = Freestream Velocity

V_V = Volume Coefficient

V_∞ = Cruising Velocity

W = Aircraft Weight

X_{np} = Location of the Neutral Point

X_{ac} = Location of the Aerodynamic Center

α = Angle of Attack

ρ = Air Density

γ = Vortex Strength

τ = Airfoil Efficiency Parameter

η = Airfoil Performance Parameter

σ = Source Strength

ω_n = Natural Frequency

ζ = Damping Ratio

Subscripts:

α = Per Unit Angle of Attack

0 = At Zero Angle of Attack

Stall = At Stall Condition

1 INTRODUCTION

For our Major Qualifying Project (MQP), the team was tasked with designing, constructing, and testing a micro aerial vehicle (MAV) to compete in the 2021 WPI MAV Competition. An MAV is a small-scale unmanned aerial vehicle (UAV). The mission requirement was to fly the aircraft from a specific takeoff/landing area, cruise for at least 2 minutes with a standardized payload, return, and land. The full problem description can be found in Section 1.3; competition rules and virtual submission requirements can be found in Appendices 2 and 3.

The primary goal of the project was to develop an MAV that adhered to the design guidelines of the competition while also scoring the maximum number of points per the scoring equation. The equation is based on time of flight, the largest straight-line dimension of the aircraft, and the number of independent inertial measurements taken. The maximum score is attained when flight time is maximized, the largest straight-line dimension is minimized, and nine inertial measurements are taken.

To approach the project, Raymer's aircraft design process (Raymer, 2018) was used as a guide. The areas of focus laid out were aerodynamics, structures, stability and control, and propulsion. To this end, groups were formed to focus on research and analysis within their respective categories. Decisions were made regarding the construction of our aircraft based on each group's findings. This report details the aircraft design and testing process. Due to Covid-19 related schedule changes, the competition was held after the report submission deadline.

1.1 Background and Literature Review

The literature review was divided into the following sub-groups: Aerodynamics, Structures, Stability and Control, and Propulsion. Each section describes different aspects of

reviewed MAVs. The review includes wing shape comparisons, material options and analysis, and methods for performance analysis.

1.1.1 Aerodynamics

Evaluating the aerodynamic performance of the MAV is critical to ensuring that it will function as it is intended to. The aerodynamic performance of the aircraft is focused primarily on the wing. Designing a wing is non-trivial and an iterative design process is required to achieve a wing design that achieves the performance requirements. A list of wing shapes, shown below in Table 1, were considered as potential candidates. Criteria for judging each wing shape included ease of construction, lift and drag performance, maneuverability at low speeds, and build envelope. Additionally, the placement of the wing was considered. A low-mounted wing gives better lift and climbing performance but is better suited for high flight speeds. A low-mounted wing would also require a more complex interface between the wing and the fuselage. A high-mounted wing is useful because the wing is more protected from the ground during takeoff and landing (Raymer, 2018). Likewise, a high-mounted wing can be easily connected to the fuselage.

Table 1. Aircraft Wing Shapes

Wing Shape	**Pros**	**Cons**
Rectangular	• Simple Construction	• Not aerodynamically efficient • High induced drag
Tapered	• Lower induced drag • Simple Construction	• Stalls at tips, wing washout required
Elliptical	• Most aerodynamically efficient shape	• Difficult to manufacture
Forward Swept	• Visually appealing	• High risk of going into a spin • Poor maneuverability

Backward Swept	• Reduced drag	• Reduced lift at slower speeds • High drag at slow speeds leading to takeoff and landing issues
Delta	• Efficiency[1] across a range of flight conditions • Simple construction	• High induced drag • High angle of attack required to achieve the required lift at slow speeds
Trapezoid	• Good flight performance • Highly efficient	• Reduced maneuverability at low speeds
Bi-plane	• Greater lift generated	• Heavy • Difficult to manufacture • Additional drag from wing mounts
Ogive	• Minimal drag at high speeds	• Difficult to manufacture • Poor low-speed performance

An MAV can utilize both a horizontal and vertical tail. The horizontal tail is only required in the absence of a reflexed airfoil. Alternatively, the elevons at the back of the wing can be trimmed to create the same effect. If a vertical tail is required for stability, the tail surface area must be calculated. The tail arm, or distance from the aerodynamic center (AC) of the tail to AC of the wing, can be approximated as 60% of the fuselage length for MAVs with front-mounted propeller engines (Raymer, 2018). Eq. 1 can be used to calculate the surface area of the tail.

$$V_v = \frac{l_v S_v}{S_W b} \qquad \text{Eq. 1}$$

[1] Efficiency, with reference to wing shape, is the amount of lift that is generated compared to the induced drag. For a wing to be efficient, the amount of lift is greater than induced drag.

V_V is the volume coefficient, l_V is the tail arm, S_V is the tail area, S_W is the wing area, and b is the wingspan (Hassanalian, Khaki, and Khosrawi, 2014). The volume coefficient ranges from 0.05-0.09, the tail generally has an aspect ratio between 1.2 and 1.8, and a taper ratio between 0.4 and 0.6 (Hassanalian and Abdelkefi, 2016).

Furthermore, extra analysis was required due to the challenge of designing wings operating in low Reynolds number conditions. Wings flying in flows with low Reynolds numbers (below 10^5) have drastically reduced aerodynamic efficiencies compared to those in higher Reynolds number flows when it comes to lift-to-drag ratios (Winslow, 2018). This is due to the stabilization of a Laminar Separation Bubble (LSB) on a wing's upper surface. This phenomenon occurs when the flow separates from the wing due to the adverse pressure gradient near the wing's leading edge. The left panel of Figure 1 illustrates this separation. This separated flow gains momentum from the free-stream flow and reattaches to the airfoil, creating a "bubble." This bubble is represented by the red streamlines in the right panel of Figure 1.

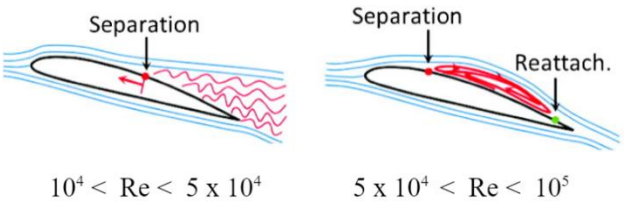

Figure 1. Laminar Separation Visualization (Winslow, 2018)

This reattachment however is now a turbulent boundary layer, usually spanning until the trailing edge of the airfoil for low angles of attack (Winslow, 2018.) As the angle of attack is increased for a particular low-Re airfoil, the end of the LSB moves towards the trailing edge of the airfoil (Winslow, 2018.) This growth allows the LSB to span over 15-40% of the chord length, causing a dramatic increase in drag and loss in lift (Winslow, 2018). Eventually, close to the stall

angle of the airfoil, the flow fluctuates between reattachment and complete separation resulting in unsteady flight characteristics and dramatic variations in pitching moment (Winslow, 2018.) The separated layer may not even reattach to form the bubble for certain combinations of low Reynold number flows and high angles of attack as seen on the left panel of Fig. 1. In addition, flows of even lower Reynold numbers, such as $< 5 \times 10^4$, will experience a laminar separation bubble even closer to the leading edge. As the Reynolds number of a flow is lowered even further, eventually the laminar separation bubble can have such detrimental effects that the airfoil is essentially stalling for most of its operational angles of attack, rendering sustained flight highly unlikely (Winslow, 2018).

1.1.2 Structures

The structure of the aircraft must be able to withstand all forces of flight without sustaining irreparable damage or being rendered inoperable between flights. These forces include lift, drag, pressure across the wing, forces from the acceleration and propulsion systems, and the force due to impact with the ground during landing. The magnitude of force changes during takeoff, flight maneuvers, and landing and as a function of location on the MAV. Structural design should be performed in a way that the locations of maximum stress like joints and edges can withstand relevant loads.

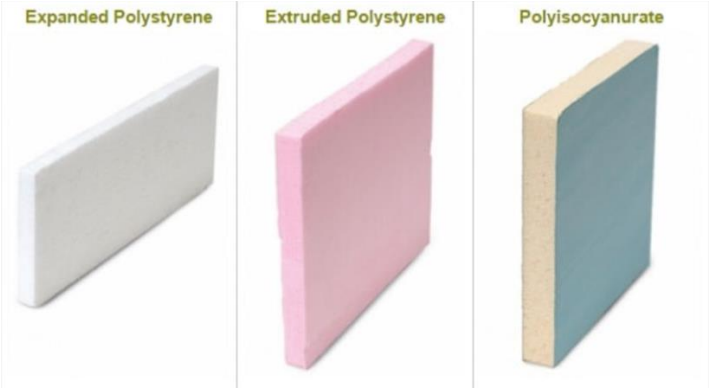

Figure 2. Typical MAV Foams (Eubanks, 2018).

Research was completed on different MAVs described in Sec. 1.1.6 and the materials used in their construction were compared. MAVs created at WPI in the past were fabricated using XPS (extruded polystyrene) foam (Carter et. al, 2005 & Henry et. al., 2001). There are three types of foam typically used in construction: expanded polystyrene, extruded polystyrene, and polyisocyanurate (Eubanks, 2018). The foams differ in density and permeability. Expanded polystyrene and polyisocyanurate have great strength to weight ratios but neither is as strong and lightweight as the extruded polystyrene. There is a range of densities available for extruded polystyrene foam and the optimal type must be chosen. In Fig. 3, the strength per unit density was plotted against the overall density for a range of XPS foams offered by *Foamular*, a brand of high-density insulation foam, to determine which foams had the best performance relative to their weight. The almost linear relationship shows that the higher-density XPS foams also offer better strength-to-weight ratios.

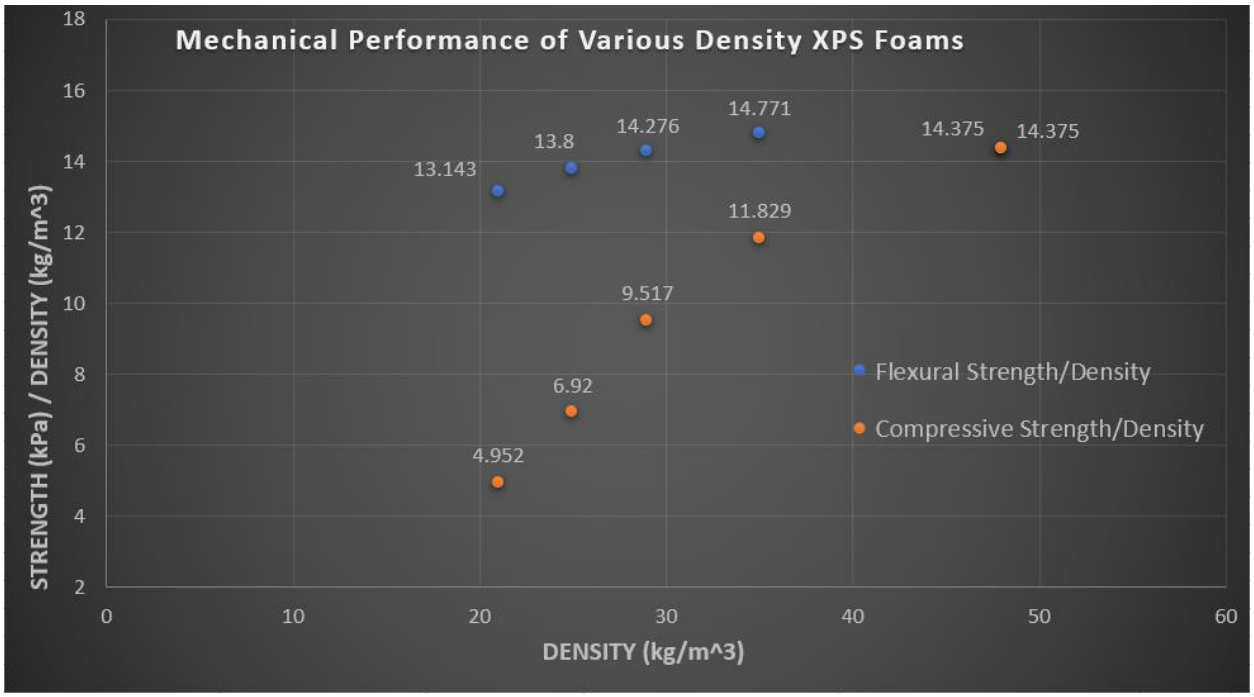

Figure 3. Various foam densities (kg/m^3) plotted for mechanical strength by flexural and compressive strength (kPa). Data source: (Corning, 2011)

Other materials considered include Styrofoam, cardboard, and balsa wood. Styrofoam and cardboard both have poor strength-to-weight ratios compared to polystyrene foam. Cardboard has been popular in creating inexpensive model drones for beginners but is not as strong as polystyrene foam. Balsa wood is good for use in creating internal structures and reinforcements due to its exceptional stiffness, low density, and heat-resistant properties. It is a softwood that is easy to work with, but it is brittle and does not smooth well (Johnson, 2002). Therefore, its use will be limited to inside foam structures and as control surfaces.

1.1.3 Stability

Stability refers to the aircraft's tendency to return to equilibrium after being disturbed. There are two types of stability: static and dynamic. Static stability is the initial tendency of an aircraft to return to its original state when disturbed. There are three kinds of static stability: positive, neutral, and negative (Cutler, 2015). For our aircraft, we wanted to achieve positive static stability, meaning that the aircraft will return to its original attitude after it is disturbed. One example of positive static stability is when the aircraft is affected by turbulence causing a nose-up attitude. When that happens, we expect our aircraft to lower the nose and return to level flight. Dynamic stability is achieved when the dynamic motions eventually return the aircraft to its original state over multiple oscillation periods, with the number of periods dependent on how damped the system is (Raymer, 2018). One example of this type of response is how the aircraft responds to a nose-up or nose-down attitude but is trimmed to level flight. Over a certain amount of time, the aircraft will return to level flight attitude instead of pitching up or down. To ensure longitudinal static stability, Eq. 2 must be satisfied (Hassanalian, Khaki, and Khosrawi, 2014). In Eq. 2, C_{m0} is the moment coefficient when the angle of attack is 0, and $\frac{\partial C_m}{\partial C_l}$ is the slope of the moment-lift curve.

$$C_{m0} > 0 \; and \; \frac{\partial C_m}{\partial C_l} < 0 \qquad \text{Eq. 2}$$

Determining the aircraft's center of gravity (CG) is critical when analyzing stability. The center of gravity must lie between the neutral point and the most forward point on an aircraft to be considered statically stable. For example, if the center of gravity is too far forward, the stability increases but the aircraft has more of a nose-down attitude. This makes landing the aircraft difficult since more back pressure on the elevator is needed. An aft center of gravity causes the aircraft to lose stability. An aircraft can take off with an aft center of gravity but as the weight of the aircraft changes, either due to fuel burn or payload decrease, this can cause the aircraft to become tail-heavy (Raymer, 2018). Thus, a stall is more likely to occur as the aircraft favors a nose-up attitude. From conducting a dynamic stability analysis, we can also determine how the aircraft will react to disturbances, which could be sudden changes in pitch, yaw, or roll. Both static and dynamic stability analyses aim to estimate how the aircraft returns to steady level flight. We can also estimate the static stability of the aircraft by using the static margin. The static margin is the distance between the center of gravity and the neutral point. If the center of gravity lies before the neutral point, the static margin is positive, and the aircraft is stable. If the static margin is negative, the aircraft is unstable and the aircraft relies on the elevator to be stable.

To relate the static margin to the center of gravity, Eq. 3 is used. Since MAVs with Zimmerman wings typically have no horizontal tail, the neutral point is located at the aerodynamic center (Hassanalian, Khaki, and Khosrawi, 2014).

$$k_n = h_o - h \qquad \text{Eq. 3}$$

In this equation, k_n is the static margin, and h_o and h are the scaled distances between a datum point and the aerodynamic center (AC) and CG, respectively. These distances are scaled by dividing by the mean aerodynamic chord (MAC). The datum is typically the leading edge of the wing at the root. The AC can be found using XFLR5 analysis, the center of gravity using SolidWorks mass analysis, and MAC for any airfoil using Eq. 4 (Hassanalian, Khaki, and Khosrawi, 2014).

$$MAC = \frac{2\mathrm{bc}_{\{\mathrm{root}\}}{}^{2}}{3S} \qquad \text{Eq. 4}$$

1.1.4 Controls

This section discusses the key elements of the MAV's controls. These include control surfaces, servos for control actuation and the flight controller module.

1.1.4.1 Control Surfaces

To better understand the purpose and functionality of control surfaces, the team researched control surfaces and sizing. When designing an aircraft there are three control surfaces to consider: the ailerons, elevator, and rudder. The ailerons control roll, the elevator controls pitch, and the rudder controls yaw. Some approximations can be used for the sizing of these control surfaces (Raymer, 2018). Table 2 depicts the control surface sizing which will be used for the design of our aircraft.

Table 2. Control Surface Area Percentages

Control Surface	**Area Percentage of Wing Planform Area**
Ailerons	10%
Elevator	40%
Rudder	35%

In an MAV, the ailerons and elevator can be combined into elevons to reduce the size and weight of the control surfaces. The ailerons work by moving in opposite directions, with the aileron that moves down having increased lift causing a roll towards the upper aileron. Elevators work by moving up or down in sync to change the pitch. As the elevators move up the lift decreases on the rear of the aircraft causing the nose to pitch up, and vice versa as the elevators move down (Federal Aviation Administration, 2016).

1.1.4.2 Servo Sizing

Servos are an important part of controlling the different control surfaces for MAVs. The team researched how to size the servos and the best method for connecting the servos to the control surface and the microcontroller. The team also researched servos that had been used in other projects. Past projects used servos with torques of 8 – 10 oz-in.

1.1.4.3 Flight Controller

The team researched what flight controller the team would use for our aircraft. A part of our team's score for the competition results from demonstrating nine inertial measurements: body-axis angular orientations (pitch, yaw, and roll), angular velocities (for pitch, yaw, and roll), aircraft x-y position, aircraft altitude, and aircraft velocity. A flight controller measures in-flight data and offers the ability to control the aircraft autonomously. From looking at past MQPs, a common brand of flight controller used was the Pixhawk. The Pixhawk series has multiple types of flight controllers; one of these controllers is the Pixhawk 4 Mini. The Pixhawk 4 Mini was ideal for our MAV since it is lightweight, and each controller comes with sensor redundancy. Sensor redundancy means that the flight controller has multiple sensors that measure similar flight data. This is valuable if one sensor is not operating properly during flight, as it lowers the possibility of control system failure. Pixhawk controllers offer GPS capability with ground control programs

using Python. The ground control programs that are compatible with the Pixhawk are QGroundControl and Mission Planner.

1.1.5 Propulsion

There are two primary modes of propulsion for MAVs: hydrocarbon fuel and electric. Since competition rules prohibit the use of combustion engines, only electric motors were explored. There are two common types of electric motors used in MAV applications: brushed and brushless DC motors. Both types of DC motors use lithium-ion polymer (LiPo) batteries as a power source.

Both brushed and brushless motors contain a rotor and a stator, but the two motors differ in how they alternate magnetic field polarity. Brushed motors use electrical commutators (brushes) that send current into the coils and produce a magnetic field. As the magnetic field interacts with the permanent magnets (stator) the rotor rotates. When the poles of the rotor and stator cross the rotor's magnetic field switches, continuing rotation. This process is controlled by the voltage across the stator. Brushless motors use a three-phase electronic speed controller (ESC) to alternate magnetic field polarity by phasing the supply current to the coils (now in the stator) to manipulate the magnetic field. In a brushless motor, the permanent magnet is used as the rotor. ESCs are also able to control the rotational speed of the motor by varying the current delivered to the coils (Winslow et. al, 2016).

Brushless DC motors are more desirable for MAV applications since the ESC increases the efficiency of the motor. The efficiency can be increased compared to a brushed motor since the ESC can change the current it delivers to the motor faster than a brushed motor can have its armature voltage changed (Winslow et. al, 2016). In addition to making the motor more efficient, ESCs also operate using pulse-width-modulated (PWM) signals, which are the same signals that

control servos. This means only one controller is required to control both the propulsion system and servos for the control surfaces (Manikanta Babu, 2016). Control-related communication occurs between a 2.4GHz transmitter on the ground and a micro-receiver inside the fuselage.

A propeller generates lift horizontally to propel the aircraft forward. They are typically two or three wings, with a high aspect ratio, which are rotated about the point at which they connect. Propellers are conventionally defined by two metrics: their diameter and their pitch. For example, an 8x6 propeller has a diameter of eight inches and a pitch of six inches. The pitch of the propeller can be thought of as how far forward the propeller's leading edge would move in one rotation if it cut perfectly through a medium with no slip. In this example, the propeller would move forward six inches for one rotation of the propeller.

Another consideration was that a fixed propeller and spinner was not possible for our design as it could get damaged during landing. Since our MAV is most likely not equipped with landing gear, it will be required to perform relatively safe belly landings. The concern is that the torque from the propeller striking the ground might damage the motor or vehicle. For this reason, the team decided to use a folding propeller, capable of folding into the MAV and coming to a complete rotational stop while exerting the minimum amount of lateral torque on the aircraft. This will likely also extend individual propeller lifetime as they are designed for crash resistance.

1.1.6 Reviewed MAVs

In addition to the wing trade study, a review of MAV designs from literature was completed. The goal of this review was to analyze the design parameters of previous projects to determine what sizing and flight performance specifications we should aim for. The MAVs, shown in Table *3,* suggest that Zimmerman and Inverse Zimmerman were popular options for similar missions. Other wing shapes researched included variations of trapezoidal, rectangular, and

elliptical wings. Based on the size of the MAV needed in this competition, aspect ratios of various wing shapes were researched as well. This research also pointed to a Zimmerman or Inverse Zimmerman being optimal to obtain the lift required. The team found that the Zimmerman wing planform is based on that of an elliptical wing, but with a smaller aspect ratio. The Zimmerman wing also has a large wing area while maintaining high aerodynamic efficiency, due to lower induced drag. The larger wing area provided by this planform has drawbacks such as increased weight. From the table, we were also able to get an idea of the type of material that was used for different MAVs. Choosing the proper material is important because the team was looking to use something lightweight and could easily be shaped to form the wing shape and fuselage that we need. Lastly, the wingspan was an important aspect to look at because we wanted to gain a general idea of how we should size our MAV. The average size of the wingspan was approximately 25 centimeters, which gave us an initial estimate of the wingspan to start our analysis.

Table 3. Design Summary of Reviewed MAVs

MAV	**Empty Weight (g)**	**Speed (m/s)**	**Wingspan (cm)**	**Flight Time (min)**	**Material**	**Wing Shape**
WPI 2001 (Henry, et al, 2001)	354	16	27.9	2	Insulation Foam	Trapezoidal Swept back
WPI 2003 (Carter, et al, 2003)	77	15	20	0.5	Foam, Balsa wood	Modified Inverse Zimmerman
WPI 2003 - (Wimbrow, et al, 2003)	113	9.5	20.3	8-10	Foam, Balsa wood	Elliptical (high wing)

Black Widow (Grasmeyer & Keennon, 2001)	50	17.8	15.2	30	Polystyrene foam	Trapezoidal
Dragonfly (Kurtulus, 2011)			30	30		Zimmerman
Dragon Slayer (Kurtulus, 2011)	300		33	35		Delta
IAI Mosquito 1 (Kurtulus, 2011)	250	12.8	33	40		Inverse Zimmerman
Var. Chamber (Kurtulus, 2011)	73		23			Mod. Zimmerman
TYTO20 (Kurtulus, 2011)	80	10	19		Fiber-carbon	Inverse Zimmerman

1.2 Project Goals

The team was tasked with creating a micro aerial vehicle (MAV) that would fulfill the requirements of the 2021 WPI MAV Competition. Points in the competition were given for three categories: time of flight, the largest straight-line dimension of the aircraft, and the number of independent inertial measurements taken per the scoring equation, Eq. 5.

$$S = 17.4\left[\frac{130.6t}{X^3} + 0.1875\sum_n A_n\right] \quad \text{Eq. 5}$$

X is the length measurement taken along the longest straight-line dimension of the aircraft in centimeters; the longer the aircraft, the lower the points scored. The aircraft must be able to carry a payload of 55 g for a specified flight time. The aircraft must be able to fly for at least two minutes; maximum points are achieved for a flight time of four minutes, equal to 240 seconds in the above equation, where time is represented by t. The aircraft must also have inertial sensors capable of measuring nine different quantities: body-axis angular orientations (pitch, yaw, and roll), angular

velocities (for pitch, yaw, and roll), aircraft x-y position, aircraft altitude, and aircraft velocity. Each measurement counts as one point, given by A_n in Eq. 5.

The goal of this project is to fulfill the requirements of the competition rules and maximize the score. It is equally important to demonstrate the group's knowledge of aerospace engineering and be able to apply that knowledge to successfully complete this project.

1.3 Project Design Requirements, Constraints, and Other Considerations

The mission requirement is to fly the micro aircraft from a specified take-off area/landing area, carry a payload for a minimum of two minutes, and return to land at the take-off/landing area. For a complete list of requirements, see the 2021 WPI MAV Competition Rules in Appendix 2: WPI Internal Competition Rules. Figure 4 shows a general diagram of the airfield layout for the competition. Due to the COVID-19 pandemic, the competition will be held virtually this year after the report submission deadline. The required flights will be recorded and included with other required information, for more information on submission specific guidelines see Appendix 3: WPI MAV Virtual Competition Rules.

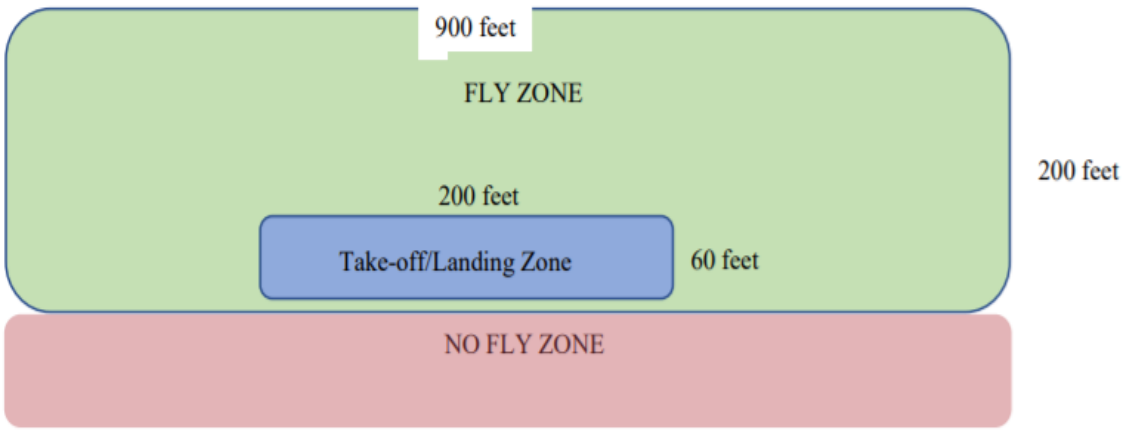

Figure 4. Airfield Layout.

The competition is judged on a scoring metric. The metric includes variables such as the maximum overall length of the aircraft (x), time of flight (t), and the number of inertial measurements taken (A_n). The time of flight variable is piecewise, given in Eq. 6. Total points earned is the sum of length, time, and inertial measurement terms.

$$\text{If } t < 120 \text{ then } t = 0$$
$$\text{If } 120 < t < 240 \text{ then } t = t \qquad \text{Eq. 6}$$
$$\text{If } t > 240 \text{ then } t = 240$$

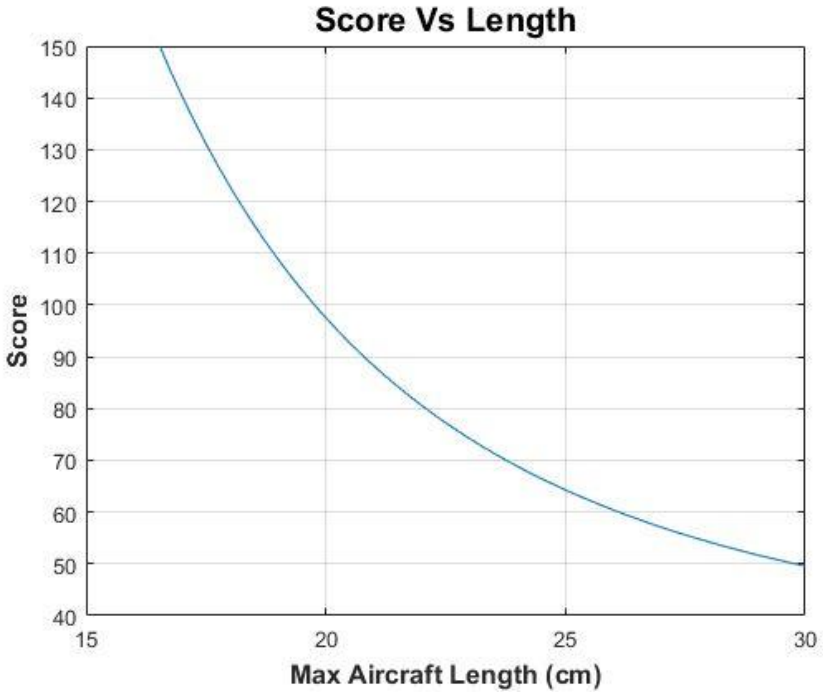

Figure 5. Score vs. Max Linear Dimension

Figure 5 shows a plot of the score as a function of the maximum linear dimension assuming maximum points for flight time and inertial measurements are achieved. The plot depicts a large increase in score when decreasing the size of the MAV. As the overall length of a competing

team's aircraft decreases, the maximum possible score increases exponentially. This metric is convenient to compare scores between teams.

1.4 Project Management

To efficiently work on our project, our team was divided into four subgroups: Aerodynamics, Structures, Controls and Stability, and Propulsion. Each group was responsible for conducting research, testing, and analysis. Table 4 is the breakdown of the four groups and responsibilities.

Table 4. Subgroup Members and Responsibilities

Subgroup	**Team Member**	**Responsibilities**
Aerodynamics	Ty Bugdin Dieter Teirlinck John Trainor	• Aerodynamic Design and Analysis • Airfoil Analysis • Calculating L/D ratios • Calculating Moments • Wing Analysis
Structures	Sophie Henehan Matthew Shriner	• Fabrication of MAV • Structural Design and Analysis
Stability and Controls	Noah Shoer Stephen Weaver	• Microcontrollers • Sensors • Stability analysis
Propulsion	Noah Shoer Dieter Teirlinck	• Choosing motors, servos, and battery • Power Analysis

1.5 MQP Objectives, Methods, and Standards

1. Create preliminary design
    a. Develop potential conceptual designs
    b. Complete literature review to narrow down design options
    c. Determine airfoil options
    d. Create CAD model using Solid Works to visualize model
2. Lift and drag analyses on the airfoil
    a. Compare airfoils to determine the ideal shape
    b. Evaluate optimal angles of attack, generate lift-to-drag curves
    c. Evaluate airfoil performance
    d. Refine design
    e. Testing models in the wind tunnel
3. Identify materials needed
    a. Complete literary review of materials used in previously constructed MAVs
    b. Perform stress tests on favored materials in the laboratory
    c. Employ strategies to improve the durability of construction materials
4. Fluid analyses on the wing
    a. Computationally evaluate fluid flow over wing shape using ANSYS Fluent
    b. Refine design
5. Stability analysis on control surfaces
    a. Complete stability and control calculations to predict flight performance
    b. Evaluate control surface areas and resulting forces using control equations
    c. Refine design

6. Physical testing
    a. Complete glide and lasso tests to evaluate stability characteristics
    b. Assess damage after glide and lasso tests to identify weak points in the structure
7. Finalize Design
    a. Reevaluate design based on flight performance
    b. Complete powered flight test
    c. Compete in WPI Competition

Standards used in this project are the following: NACA, Eppler, Gottingen, and Selig airfoils.

1.6 MQP Tasks and Timetable

Figure 6 is the schedule for major objectives for the team.

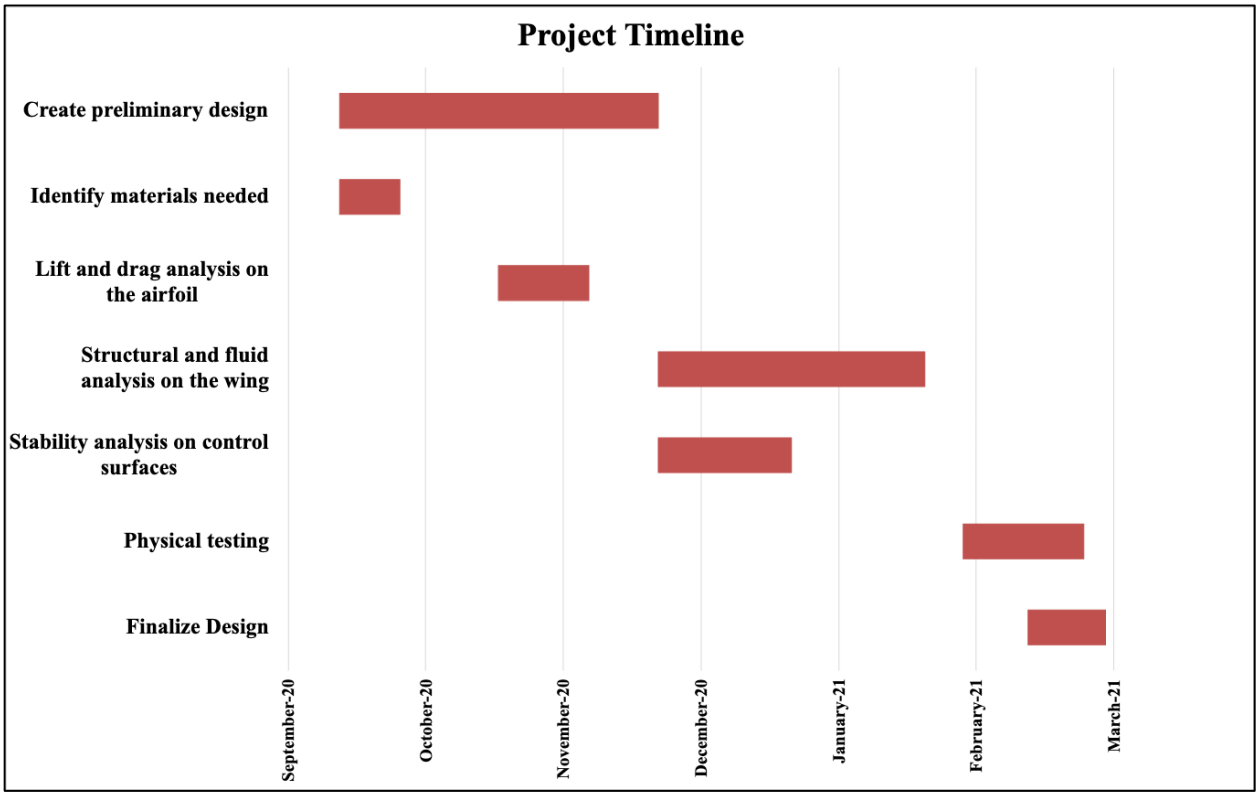

Figure 6: Gantt Chart of Project Schedule

1.7 Specifications and Design Summary

Table 5: Design Specifications

Type of Wing	Zimmerman
Airfoil	Selig 2027
Chord Length	25.4 cm
Wingspan	36.8 cm
Battery Capacity	Lumenier 1000mAh 3s 35c LiPo
Motor	E-flite Park 370 Brushless Outrunner Motor
Motor Kv	1360 Kv
Propeller	Hobby King 9x6 Folding Propeller
Servo Motor	Tiankongrc SG90 24.997 oz-in

Table 6: Weight Buildup List

Item	Payload Configuration Weight (g)	Pixhawk Configuration Weight (g)
Foam structure	165.6	165.6
Motor	37	37
Motor Mount	20	20
Battery	92.6	92.6
Servo Motors	18	18
Push Rods	3	3
Propeller	10	10
ECS	10.5	10.5
Micro Receiver	7	7
Payload	50	X
Pixhawk	X	36.9
Pixhawk PDB	X	8.5
Pixhawk GPS	X	32.8
Total Weight	**413.7**	**441.9**

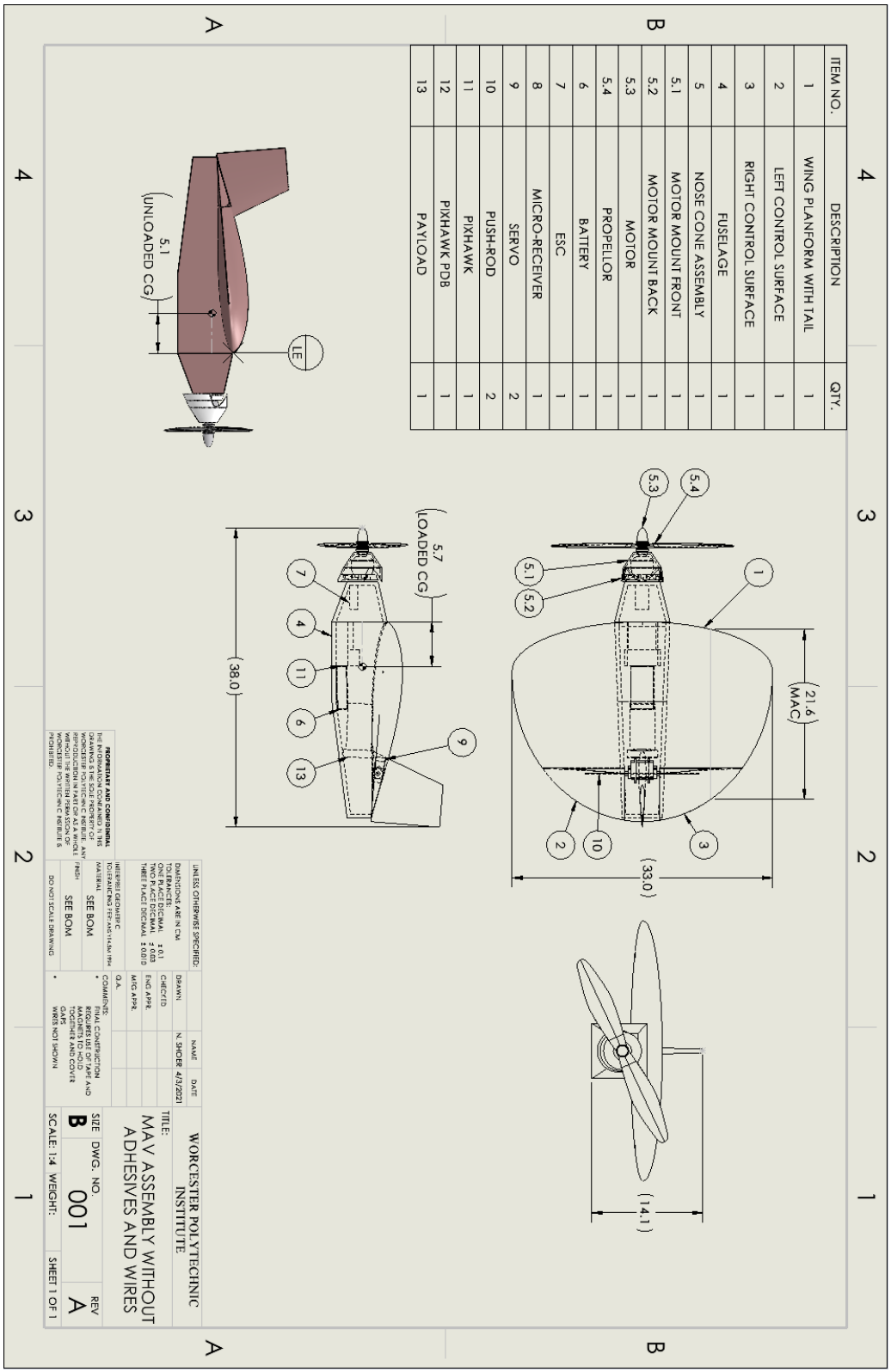

Figure 7. Final MAV Design Drawing

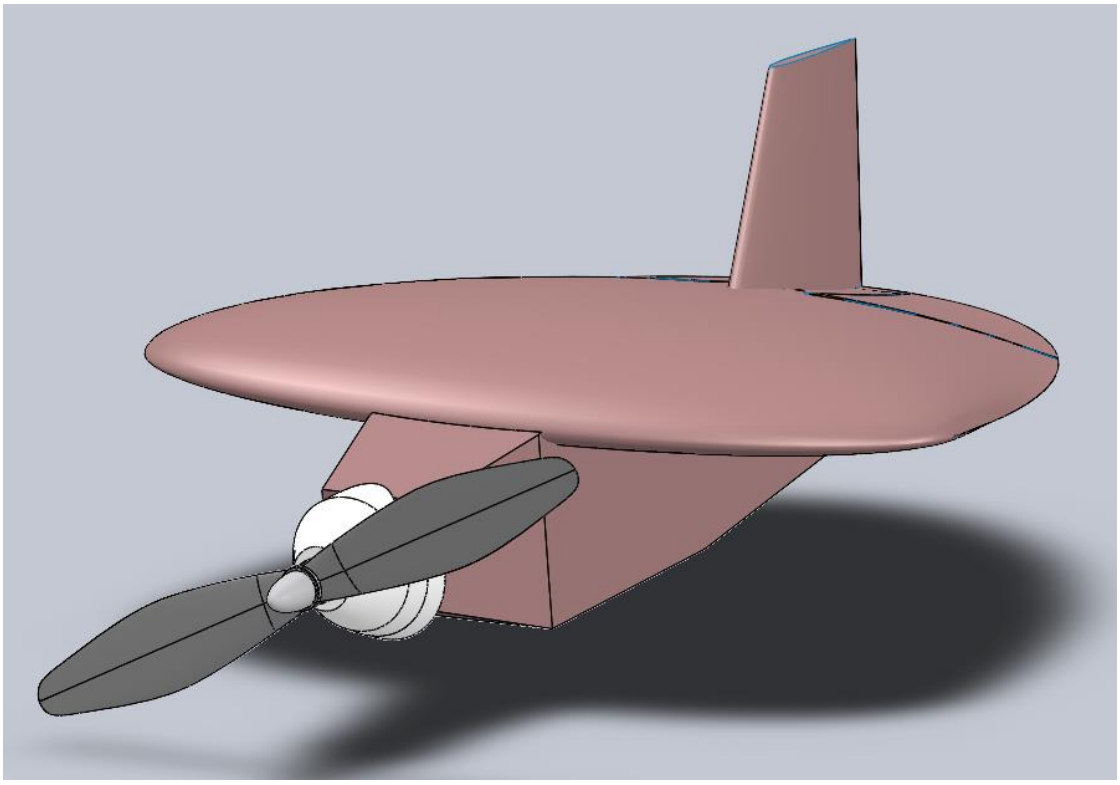

Figure 8. CAD Model of Final MAV Design

Figure 9: Completed MAV

2 PRELIMINARY DESIGN AND ANALYSIS

This section details the preliminary design and analysis that was completed to develop an initial MAV concept. A selection process was completed to obtain an airfoil that would achieve the necessary aerodynamic requirements. The shape and basic dimensions of the wing were determined. Conceptual designs for the MAV's fuselage were created in CAD. Finally, the static and dynamic stability of the wing shape was evaluated.

2.1 Airfoils

Before performing any aerodynamic analysis, we determined target values for the wing's dimensions. Due to the initial uncertainty in our vehicle mass, a range of masses were considered. Initial estimates of the vehicle mass were between 150g and 560g. To maximize efficiency, an aircraft should cruise at the velocity at which the lift-to-drag ratio is maximized (Raymer, 2018). The lift-to-drag ratio (Eq. 7) can be calculated as the ratio between the lift and drag coefficients

$$\frac{\mathrm{L}}{\mathrm{D}} = \frac{\mathrm{C_L}}{\mathrm{C_D}}, \qquad \text{Eq. 7}$$

where,

$$\mathrm{C_L} = \frac{\mathrm{W}}{\frac{1}{2}\rho_\infty \mathrm{V}_\infty^2 \mathrm{S}}, \qquad \text{Eq. 8}$$

$$\mathrm{C_D} = \mathrm{C_{D_0}} + \mathrm{K}\mathrm{C_L}^2, \qquad \text{Eq. 9}$$

$$\mathrm{K} = \frac{4}{3}\frac{1}{\pi \mathrm{eAR}}. \qquad \text{Eq. 10}$$

The lift coefficient is a function of the vehicle weight W, the dynamic pressure $\frac{1}{2}\rho_\infty {V_\infty}^2$, and the wing area S. The drag coefficient is comprised of the parasitic drag $\mathrm{C_{D_0}}$ and the induced drag which scales with the square of the lift coefficient. The coefficient K is the induced drag factor which is

a function of the wing's aspect ratio AR and the Oswald efficiency factor e. From Eq. 10, the induced drag can be reduced by increasing the wing's aspect ratio or the Oswald efficiency factor. For our aircraft, the aspect ratio will be low to maximize the wing area while keeping the maximum linear dimension small. The maximum lift-to-drag ratio, which can be derived by taking the derivative of the lift-to-drag ratio with respect to the lift coefficient, reduces to an equation that depends only on the parasitic drag and induced drag factor as seen in Eq. 11.

$$\left(\frac{L}{D}\right)_{max} = \frac{1}{\sqrt{4C_{D_0}K}}. \quad \text{Eq. 11}$$

Likewise, the velocity at which this maximum occurs can be calculated using Eq. 12.

$$V_{\left(\frac{L}{D}\right)_{max}} = \sqrt{\frac{2}{\rho_\infty}\frac{W}{S}\sqrt{\frac{K}{C_{D_0}}}}. \quad \text{Eq. 12}$$

In Eq. 12, $\frac{W}{S}$ is the wing loading, which is critical to the structural design of the wing. The air density $\rho_\infty$was assumed to be 1.225 kg-m^{-3}, which corresponds to the density of air at sea-level, for all relevant calculations. The competition rules specify that the aircraft's altitude is not to exceed 100 m. The change in air density at 100 m from that at sea level is negligible. To obtain lift-to-drag and velocity values in terms of the dimensions of the wing, namely the wingspan, b, and the aspect ratio, AR, the relationship in Eq. 13 is used.

$$AR = \frac{b^2}{S}. \quad \text{Eq. 13}$$

Figure 10 shows how the lift-to-drag performance of a wing can vary based on aspect ratio and Oswald efficiency factor; the latter being governed primarily by the planform shape. A value of 0.02 was used for C_{D_0}, which was a realistic estimate based on aircrafts from the literature

review. For the MAV, an aspect ratio less than 1 would not be suitable as a fuselage wide enough to house the electronics and payload would likely cover too much of the wing area. Likewise, aspect ratios of 3 or more require a larger wingspan to achieve the same wing area, making it less competitive. Therefore, the aspect ratio of our wing would be between 1 and 2, or approximately 1.5.

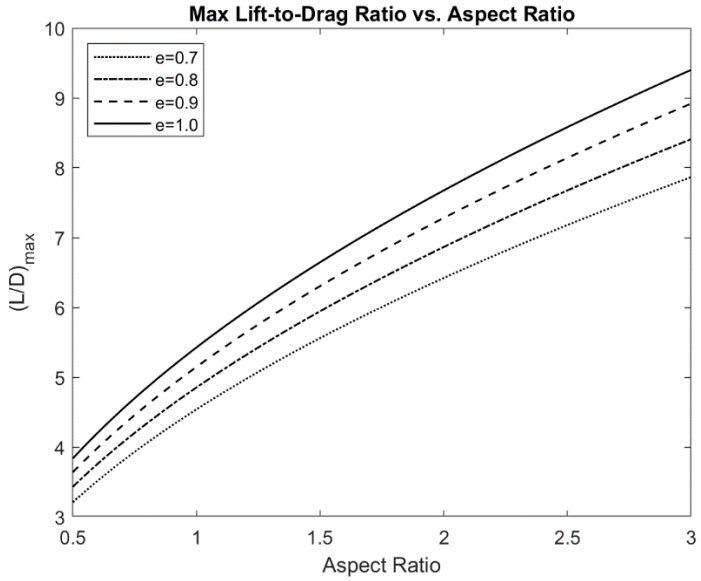

Figure 10. Maximum Lift-to-Drag Ratio vs. Aspect Ratio

Figure 11 illustrates the effects of the mass and wingspan on cruising velocity $\left(V_{\left(\frac{L}{D}\right),max}\right)$ and wing loading $\left(\frac{W}{S}\right)$. From Figure 11b, the wing loading increases significantly as the mass increases. Similarly, the differences between the wingspans grow as the mass increases. From Figure 11, it can be concluded that the ideal wingspan of those plotted is 30 cm. Using this wingspan, the cruising velocity as well as wing loading can be minimized. Furthermore, this wingspan still results in a competitive score if it were the largest linear dimension, and all other criteria were met (resulting in approximately 49.6 points).

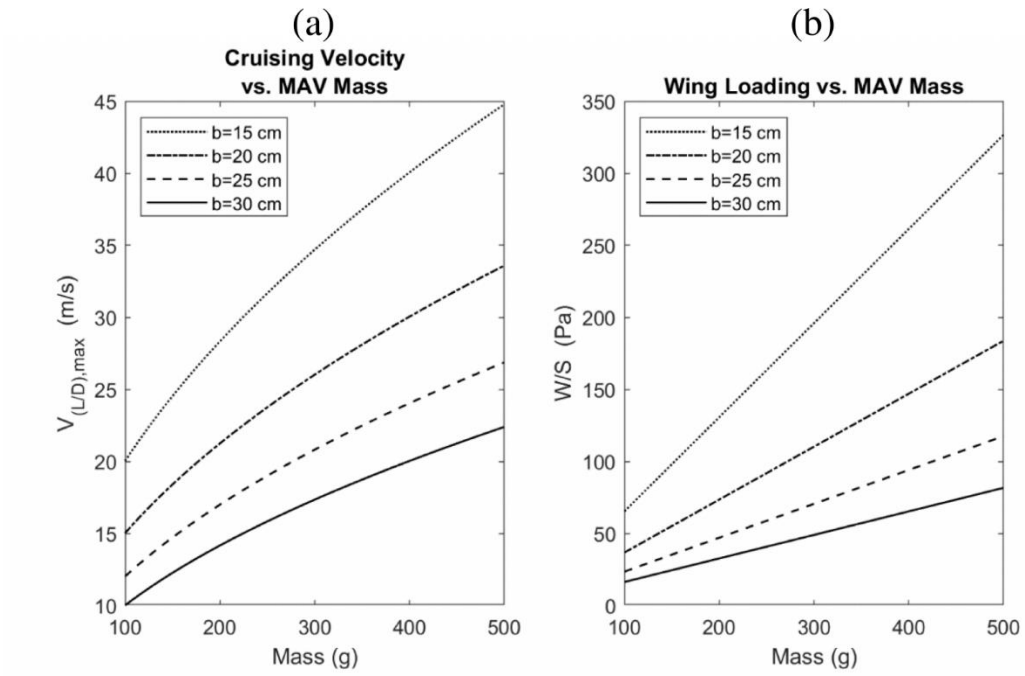

Figure 11. (a) Cruising Velocity & (b) Wing Loading vs. MAV Mass for different wingspans

From Figure 11 the target mass range of the MAV could be determined. Achieving a mass of less than 200 g is unlikely due to the mass of the payload and necessary electronics, which leaves little room for the mass of the structure. Similarly, a mass exceeding 400 g can negatively affect the efficiency of the MAV and pose risks of severe damage in the event of an accident, such as a crash or drop. Thus, we aimed to constrain the MAV mass between 250 g and 350 g. For MAV mass within this range, having an aspect ratio of 1.5, and a wingspan of 30 cm, the cruising velocity was between 16 and 19 m/s. Using Eq. 8, this corresponds to a lift coefficient of 0.26.

All airfoil analyses were completed using XFLR5, which is a low Reynolds number aerodynamic analysis tool for 2D airfoil analysis and 3D analysis of finite wings. XLFR5 uses XFOIL to solve for the pressure coefficient distribution over the airfoil via a coupled inviscid/viscous iterative solver (Drela, 1989). The inviscid flow field is determined using a combined vortex and source panel method by solving Eq. 14.

$$\Psi(x,y) = u_\infty x + v_\infty y + \frac{1}{2\pi}\int \gamma(s)\ln r(s,x,y)\,ds + \frac{1}{2\pi}\int \sigma(s)\ln\theta(s,x,y)\,ds \qquad \text{Eq. 14}$$

In Eq. 14 u_∞ and v_∞ are the components of the freestream velocity, γ is the vortex strength on the airfoil surface, and σ is the source strength on the airfoil surface. Here, the components of the freestream velocity, x- and y-coordinates, and panel lengths, s, are known. The vortex and source strengths are unknown. The program solves an additional set of equations, not shown here, which are included to account for viscous effects such as boundary layers and separation. To solve the set of equations, the equations must be discretized. The airfoil, which is a continuous curve, is discretized into a series of flat panels, as illustrated in Figure 12.

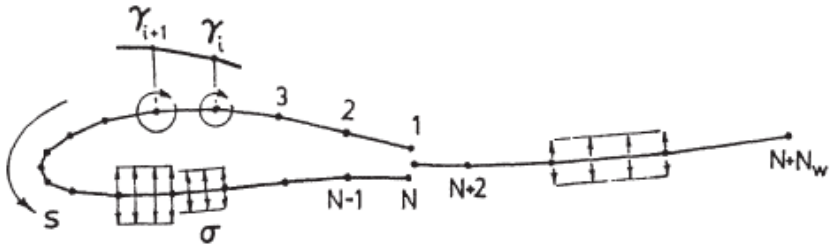

Figure 12. XFOIL Airfoil Discretization (Drela, 1989)

The discretization of the airfoil is performed automatically. To better capture the airfoil's curvature, particularly near the leading and trailing edges, additional panels can be added manually in XFLR5. Within XFLR5, four- and five-digit NACA airfoils can be generated automatically. Likewise, airfoil coordinates can be imported into XFLR5 from external sources. The initial selection of airfoils that were analyzed consisted of a large variety of NACA, Eppler, and Selig airfoils. Each airfoil has unique aerodynamic properties, which were computed in XFLR5. To filter through the raw aerodynamic data that was produced, two airfoil scoring equations for airfoil efficiency (τ), Eq. 15, and airfoil performance (η), Eq. 16, were used (Shams, 2020).

$$\tau = \left(\frac{C_l}{C_{dmax}} + \frac{C_l^{\frac{3}{2}}}{C_{dmax}} + \frac{C_l^{\frac{1}{2}}}{C_{dmax}} + C_{l0} + C_{lmax} + \alpha_{stall} + C_{l\alpha} + C_{d0} + C_{m\alpha} + C_{m0} \right) \quad \text{Eq. 15}$$

$$\eta = 0.125\frac{C_l}{C_{dmax}} + 0.250\frac{C_l^{\frac{3}{2}}}{C_{dmax}} + 0.625\frac{C_l^{\frac{1}{2}}}{C_{dmax}} \quad \text{Eq. 16}$$

These equations include several airfoil parameters including aerodynamic and stability coefficients. The first three terms in Eq. 15 include lift coefficients with varying exponentials based on different stages of the flight leg. C_l corresponds to the lift coefficient at minimum glide angle and therefore maximum range; $C_l^{\frac{3}{2}}$ corresponds to the lift coefficient at minimum power and maximum endurance; $C_l^{\frac{1}{2}}$ corresponds to the lift coefficient at optimum cruise speed (Shams, 2020). Stability coefficients ($C_{l0}, C_{lmax}, \alpha_{stall}, C_{l\alpha}, C_{d0}, C_{m\alpha}, C_{m0}$) were added in Eq. 16 as aerodynamic efficiency alone is not sufficient for wing design; stability is a necessary criterion.

Similarly, Eq. 16 weighs each coefficient with respect to their individual duration of the mission to determine aerodynamic performance at each interval. Each fraction is multiplied by a weighted value corresponding to the time the vehicle spends in each leg of the mission. Based on a four-minute flight mission, 30 seconds of glide time corresponds to a weighting factor of 0.125; 3.5 minutes of cruise time corresponds to a weighting factor of 0.625; 1 minute of flight at minimum power setting corresponds to a weighting factor of 0.250.

Airfoil efficiency (τ) and performance (η) parameters were calculated for 40 different airfoils. Since these equations may result in different optimum airfoils, the average of τ and η may be taken for an overall average score to determine the airfoil. From these equations, our airfoil choice became the Selig 2046, representing the highest score. The full list of airfoils and their respective scores, which are the averaged sums of τ and η, are tabulated in Appendix 3. The lift curve for this airfoil is plotted in Figure 13.

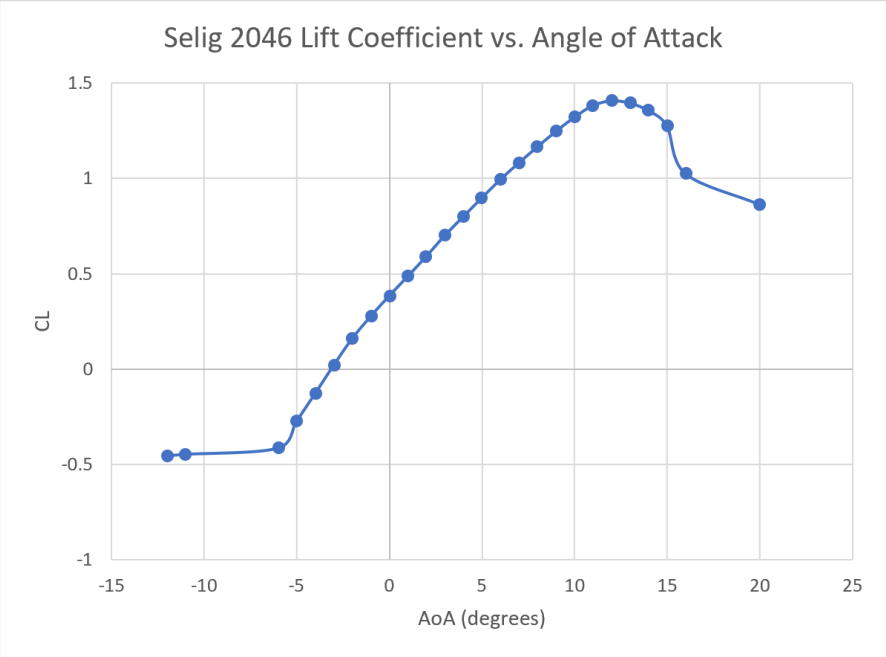

Figure 13. Selig 2046 Lift Curve

2.2 Planforms

From our wing shape trade study and literature review, we determined that a Zimmerman wing was the best option for our design. The Zimmerman wing planform allows for a large wing area and a small wingspan. A Zimmerman wing is essentially an elliptical wing with a low aspect ratio. As such, a Zimmerman wing will have the same aerodynamic efficiency characteristics as an elliptical wing. Both elliptical and Zimmerman wings have Oswald efficiency factors of 1 due to their elliptical lift distribution (Raymer, 2018). In comparison, wings with non-elliptical lift distributions have an Oswald efficiency factor between 0.7 and 0.85 (Raymer, 2018). Figure 10 demonstrated that an Oswald efficiency factor will result in a greater maximum lift-to-drag ratio.

XFLR5 was used to perform finite wing analyses. XFLR5 can determine lift distributions over finite wings using one of three different methods: lifting line theory (LLT), vortex lattice method (VLM), and the 3D panel method. Our analyses were completed using VLM. To perform

an analysis on a finite wing, drag polar data must first be calculated for the 2D airfoil being used. A wide range of Reynolds numbers and angles of attack must be considered to gather enough drag-polar data for interpolation. Occasionally the 2D solver may produce nonsensical results for a particular Reynolds number. Nonsensical values normally appear as extremely large lift-to-drag ratios and must be deleted prior to performing any 3D analysis.

Generating a Zimmerman wing in XLFR5 is a tedious process, as the chord length and offset must be calculated for each section. Within XLFR5, however, instructions can be imported to construct planforms automatically. As such, a python code was developed to generate instructions files that can be imported into XLFR5. The input parameters were the wingspan, aspect ratio, and airfoil name. The code used a simple loop to generate the planform instructions section-by-section. For a Zimmerman wing and elliptical wing, it is important to consider that chord length approaches zero as the wingtip is approached. However, a chord length of 0 will result in a singular matrix that cannot be solved by the VLM solver. Therefore, the wingtip geometry must be approximated using sections with small, non-zero chord lengths. A simple way to ease the effects of this problem and approximate the wingtip geometry is to scale up the wing. Instead of using a wing with a span of 20 cm, a wing with a span of 100 cm was used. By doing so, the wingtip could be approximated using a larger airfoil. Additionally, the section width must be refined as the wingtip is approached. This refinement can be seen in Figure 14. Values from the finite wing analyses were used in the airfoil selection process described in Section 2.1.

(a) (b)

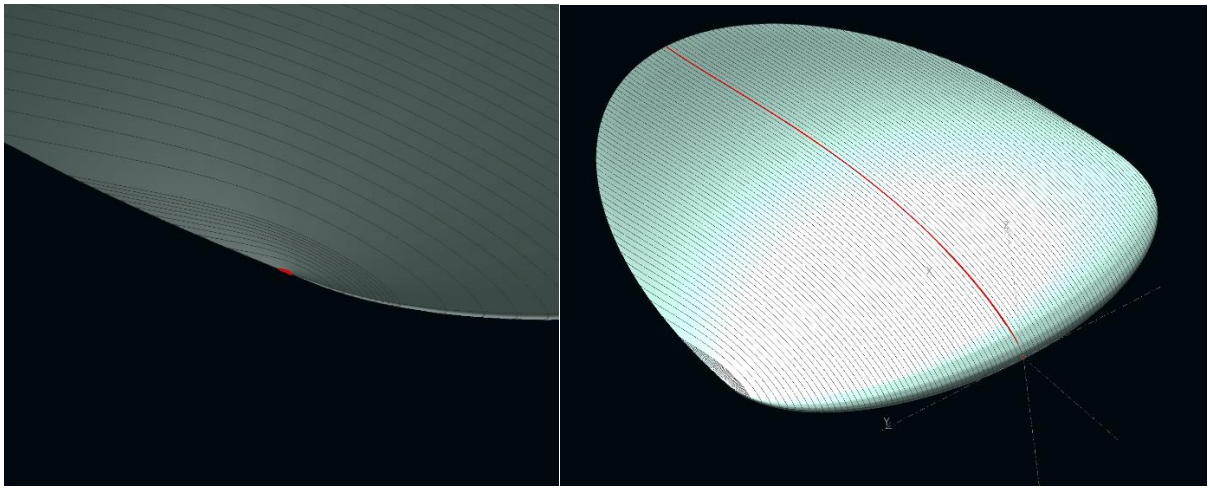

Figure 14. (a) Zimmerman Wingtip Refinement & (b) Full Wing

2.3 Conceptual Fuselage Designs

The initial fuselage design was based on a connected fuselage design (Hassanalian and Abdelkefi, 2014). The CAD model in Figure 15 was designed to fit the chosen Zimmerman planform specifications. This model was an initial design, where the height and width of the fuselage are equal to 15% of the wingspan. One design flaw of this fuselage is the obstruction to the airflow caused by attaching the fuselage to the front of the wing and preventing smooth flow over the center of the wing.

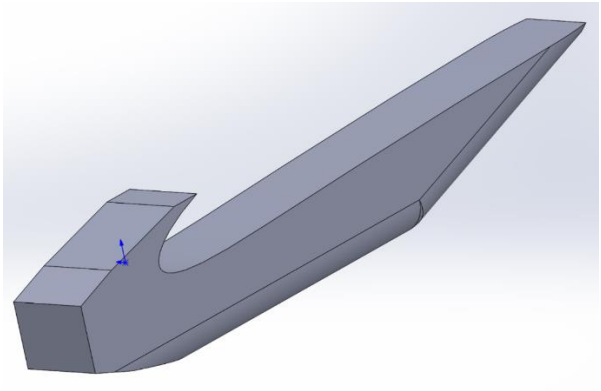

Figure 15. Initial Fuselage Conceptual Design

To minimize airflow obstructions caused by the fuselage and to reduce the drag, a new one was designed that could be integrated into the airfoil. Instead of the planform fitting into the fuselage, the fuselage fit into the wing. This new fuselage is shown in Figure 16. The planform clips into the fuselage between the curve of the airfoil and the ledge over the electronics compartment. The wing had cuts taken out of the front and bottom to interface with this new fuselage as seen in Figure 17. Figure 18 shows the Zimmerman wing attached to the fuselage.

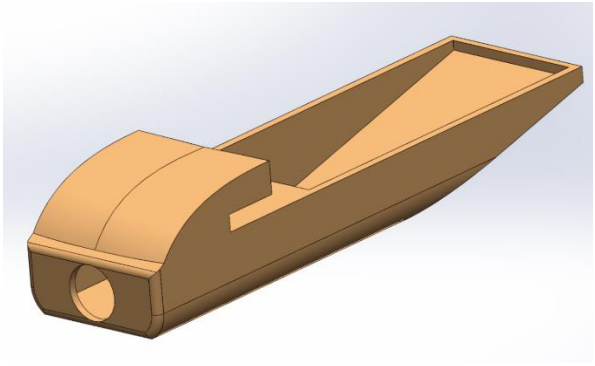

Figure 16. Second Fuselage Conceptual Design

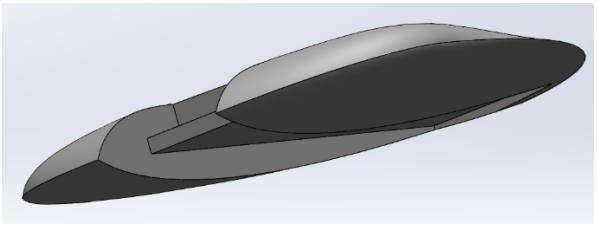

Figure 17. Modified Wing for Fuselage

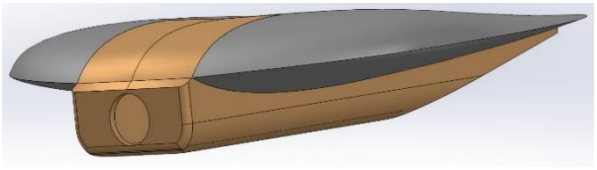

Figure 18. Conceptual Wing and Fuselage

One main issue with this fuselage design is securing it to the wing. With the initial design, it can simply be glued onto the wing, but the new one must be clipped in and secured. Two options

were proposed: using a buckle mechanism in the wing and using a dowel in the back to prevent rotation once the fuselage is slid into position. Since the wing is made of foam, the fuselage cannot be connected by screws and must have a reversible locking mechanism to enable access to the electronics components.

Neither of these fuselage designs accounted for carrying the payload, but the second design had enough space on the inside to place the payload within the fuselage. This made the second fuselage design more desirable since it could fit the payload, but this further necessitated the need for a locking mechanism to swap the payload with the inertial measurement unit in between competition flights.

2.4 Stability

This section discusses the static and dynamic stability analyses, as well as their impacts on the design and flight.

2.4.1 Static Stability

To determine if our aircraft was statically stable, the center of gravity was calculated and compared to the neutral point. To be considered statically stable, the center of gravity must lie ahead of the neutral point. This also means that the static margin—the distance between the center of gravity and the neutral point—must be positive. The center of gravity was found theoretically using both the center of gravity equation and comparing it to the SolidWorks model.

The equation used for finding the location of the center of gravity is given by Eq. 17.

$$X_{CG} = \sum \frac{W_i X_{CG_i}}{W_i}. \qquad \text{Eq. 17}$$

For this equation, the location of the center of gravity was found by taking the sum of the weights of the individual components of the aircraft (wings, vertical tail, servos, etc.) multiplied by the center of gravity of the individual components divided by the weights. The next step was to find

the neutral point. Since the team was designing a flying wing, it was assumed that the neutral point is equal to the aerodynamic center. The aerodynamic center is equal to 1/4th of the chord of the aircraft. Eq. 18 shows the relationship between the neutral point and the aerodynamic center.

$$X_{np} = X_{ac} = \frac{c}{4} \qquad \text{Eq. 18}$$

After the location of the center of gravity and the neutral point, the static margin can be found and display the stability of our aircraft. The team was using an aspect ratio from 1 to 3, so the change in the static margin was compared to the change aspect ratio. Using MATLAB, Figure 19 was created to represent the initial changes in the static margin and aspect ratio.

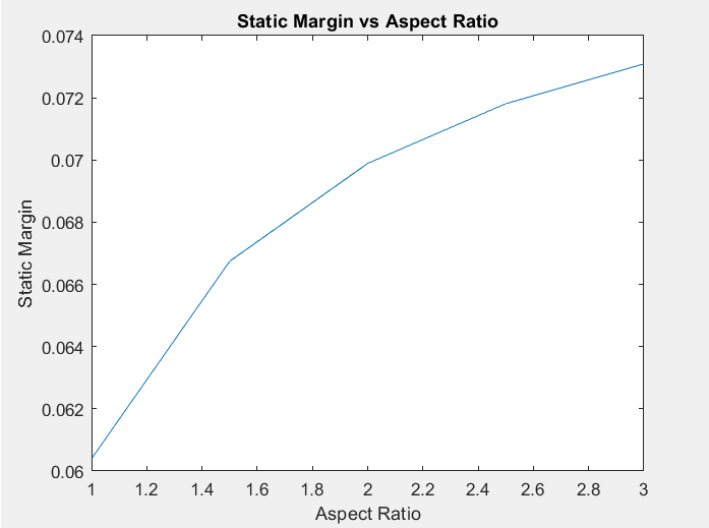

Figure 19. Static Margin vs. Aspect Ratio

Overall, the aircraft is statically stable at aspect ratios from 1 to 3, with the static margin being positive. However, this also means that the aircraft will be nose heavy. Control surfaces can be used to balance the weight.

2.4.2 Dynamic Stability

Dynamic stability is characterized by an aircraft's response to disturbances from steady-state flight. An analysis of a Zimmerman wing's longitudinal and lateral dynamic stability is

presented. Dynamic stability was evaluated for Zimmerman wings using our top three airfoil choices from the analysis in Section 2.1. The effect of aspect ratio on the dynamic stability was also investigated. This analysis was conducted using the stability analysis tools in XFLR5.

2.4.2.1 Longitudinal Stability

An aircraft's longitudinal stability refers to its stability about its pitch axis. Aircraft display two longitudinal dynamic modes of motion: phugoid motion and short period motion. Phugoid motion is characterized by slow oscillations with relatively low damping (Yechout et al., 2003). Conversely, short period motion is characterized by oscillations of a high natural frequency with a higher amount of damping (Yechout et al., 2003). Figure 20 shows that an aircraft in short period motion will typically settle faster than one in phugoid motion.

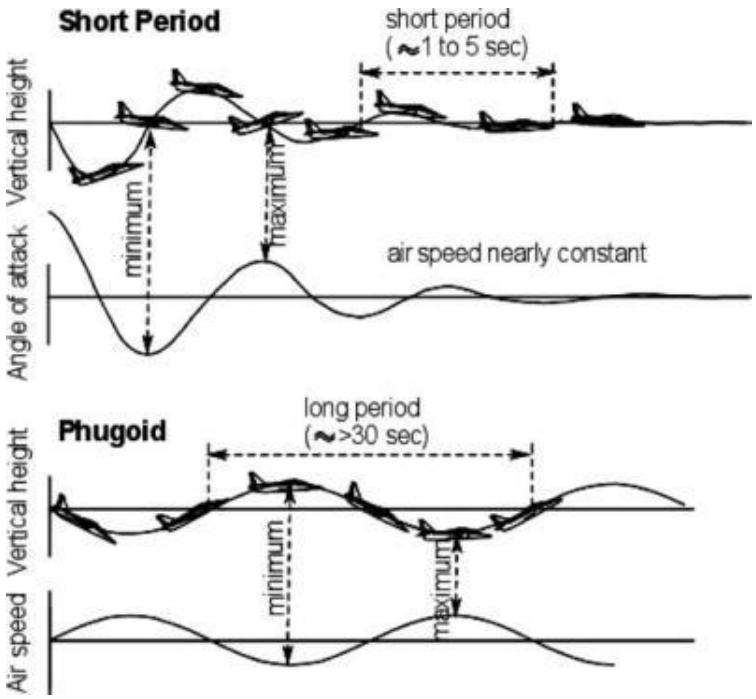

Figure 20. Short Period vs. Phugoid Motion

These modes are represented by eigenvalues, which are obtained from the linearized equations of longitudinal motion (Yechout et al., 2003). These eigenvalues consist of a real $Re(\lambda)$ and imaginary $Im(\lambda)$ component:

$$\lambda_{1,2} = -\zeta\omega_n \pm \omega_n\sqrt{1-\zeta^2} \quad \text{Eq. 19}$$

$$Re(\lambda) = -\zeta\omega_n \quad \text{Eq. 20}$$

$$Im(\lambda) = \pm\omega_n\sqrt{1-\zeta^2} \quad \text{Eq. 21}$$

λ represents the eigenvalues, ω_n is the natural frequency, and ζ is the damping ratio. The real component represents the amount of damping, which is direct indication of the wing's stability. If the real component is negative, then the system is stable. This means that the wing will settle after being perturbed. Conversely, a positive real component will result in an unstable system. The imaginary component represents the damped natural frequency.

Using XFLR5, the short period and phugoid eigenvalues were determined and tabulated for the Selig 2046, Selig 2027, and Eppler 328 airfoils in Table 7, Table 8, and Table 9 respectively. For both the short period modes and the phugoid modes, the differences in settling times between aspect ratios were minimal. One issue is the positive real values for the second phugoid values. Positive real values indicate instability; therefore, the aircraft may not return to steady flight. This can be adjusted by applying trim to the elevons of the aircraft. Using a basic t-test, the effects of the wing's aspect ratio on longitudinal stability were statistically insignificant. The results also show that the differences in stability between the three airfoils studied were minimal.

Table 7. Longitudinal Stability Modes for s2046 (XFLR5)

Short Period Motion, s2046 Airfoil				
Aspect Ratio	Short Period Mode		Settling Time (seconds)	
1	-42.0211 ± 31.0264i		.0951	
1.5	-35.6539 ± 27.5348i		.112	
2	-31.3903 ± 23.2967i		.127	
Phugoid Motion, s2046 Airfoil				
Aspect Ratio	Phugoid Mode	Settling Time (seconds)	Phugoid Mode	Settling Time (seconds)
1	-3.3911 ± 0i	1.180	1.7114 ± 0i	N/A
1.5	-3.9718 ± 0i	1.007	2.3599 ± 0i	N/A
2	-4.6901 ± 0i	.853	2.9705 ± 0i	N/A

Table 8. Longitudinal Stability Modes for s2027 (XFLR5)

Short Period Motion, s2027 Airfoil				
Aspect Ratio	Short Period Mode		Settling Time (seconds)	
1	-53.5876 ± 40.0162i		.0746	
1.5	-45.6257 ± 35.4831i		.0877	
2	-40.3202 ± 29.7608i		.0992	
Phugoid Motion, s2027 Airfoil				
Aspect Ratio	Phugoid Mode	Settling Time (seconds)	Phugoid Mode	Settling Time (seconds)
1	-2.5364 ± 0i	1.577	1.4804 ± 0i	N/A
1.5	-3.0073 ± 0i	1.330	2.0230 ± 0i	N/A
2	-3.5551 ± 0i	1.126	2.5623 ± 0i	N/A

Table 9. Longitudinal Stability Modes for Eppler 328 (XFLR5)

Short Period Motion, Eppler 328 Airfoil				
Aspect Ratio	Short Period Mode		Settling Time (seconds)	
1	-80.9961 ± 63.0281i		.0494	
1.5	-69.7643 ± 55.5608i		.0573	
2	-62.1416 ± 45.7610i		.0644	
Phugoid Motion, Eppler 328 Airfoil				
Aspect Ratio	Phugoid Mode	Settling Time (seconds)	Phugoid Mode	Settling Time (seconds)
1	-1.8618 ± 0i	2.148	.8587 ± 0i	N/A
1.5	-1.9341 ± 0i	2.068	1.3403 ± 0i	N/A
2	-2.4279 ± 0i	.824	1.6103 ± 0i	N/A

2.4.2.2 Lateral Stability

An aircraft's lateral stability refers to its stability about its roll and yaw axes. As with longitudinal motion, aircraft display three types of lateral dynamic modes: roll, Dutch roll, and spiral. The roll mode represents the aircraft's tendency to purely roll back and forth and is typically stable at low angles of attack (Yechout et al., 2003). The spiral mode is characterized by a slow roll and yawing motion and appears as a descending turn (Yechout et al., 2003). However, the spiral mode is generally unstable and requires pilot input to prevent critical instability. The Dutch roll mode involves oscillations in the aircraft's yaw and roll angles, as well as in its sideslip (Yechout et al., 2003). Figure 21 illustrates an aircraft's behavior in Dutch roll motion.

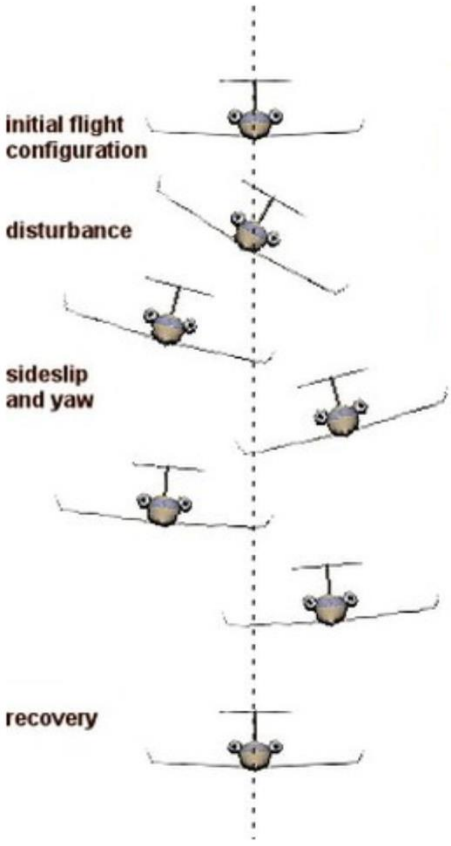

Figure 21. Dutch Roll Mode

Like the longitudinal modes, the lateral modes are represented by eigenvalues, which are obtained from the linearized equations of lateral motion. Using XFLR5, the eigenvalues representing the three lateral dynamic modes were determined and tabulated for the s2046, s2027, and Eppler 328 airfoils in Table 10, Table 11, and Table 12 respectively . For each of the three aspect ratios investigated, the spiral mode is unstable. Additionally, some of the Dutch roll modes are observed to have a large settling time or be unstable altogether. Therefore, additional lateral stabilization will be required in the form of a vertical stabilizer. Using a t-test, the effect of the wing's aspect ratio on the roll and stable Dutch roll modes are statistically insignificant. Once again, the differences in stability between the three airfoils studied are minimal.

Table 10. Lateral Stability Modes for s2046 (XFLR5)

Roll and Spiral Motion, s2046 Airfoil				
Aspect Ratio	Roll Mode	Settling Time (seconds)	Spiral Mode	Settling Time (seconds)
1	-18.3609 ± 0i	.218	2.1401 ± 0i	N/A
1.5	-18.9850 ± 0i	.211	1.8258 ± 0i	N/A
2	-19.7432 ± 0i	.203	1.6012 ± 0i	N/A
Dutch Roll Motion, s2046 Airfoil				
Aspect Ratio	Dutch Roll Mode	Settling Time (seconds)	Dutch Roll Mode	Settling Time (seconds)
1	-4.2882 ± 0i	.933	.1332 ± 0i	N/A
1.5	-3.9596 ± 0i	1.010	-.0992 ± 0i	40.323
2	-3.5775 ± 0i	1.118	-.2473 ± 0i	16.175

Table 11. Lateral Stability Modes for s2027 (XFLR5)

Roll & Spiral Motion, s2027 Airfoil				
Aspect Ratio	Roll Mode	Settling Time (seconds)	Spiral Mode	Settling Time (seconds)
1	-25.0943 ± 0i	.159	1.4804 ± 0i	N/A
1.5	-26.6001 ± 0i	.150	1.7334 ± 0i	N/A
2	-27.7359 ± 0i	.144	1.4510 ± 0i	N/A
Dutch Roll Motion, s2027 Airfoil				
Aspect Ratio	Dutch Roll Mode	Settling Time (seconds)	Dutch Roll Mode	Settling Time (seconds)
1	-4.2882 ± 0i	.933	.1332 ± 0i	N/A
1.5	-2.5332 ± 0i	1.579	.0465 ± 0i	N/A
2	-2.0400 ± 0i	1.961	-.2780 ± 0i	14.388

Table 12. Lateral Stability Modes for Eppler 328 (XFLR5)

Roll & Spiral Motion, Eppler 328 Airfoil				
Aspect Ratio	Roll Mode	Settling Time (seconds)	Spiral Mode	Settling Time (seconds)
1	-47.8067 ± 0i	.0837	1.4642 ± 0i	N/A
1.5	-44.8620 ± 0i	.0892	1.1897 ± 0i	N/A
2	-47.1484 ± 0i	.0848	1.1068 ± 0i	N/A
Dutch Roll Motion, Eppler 328 Airfoil				
Aspect Ratio	Dutch Roll Mode	Settling Time (seconds)	Dutch Roll Mode	Settling Time (seconds)
1	-1.7741 ± 0i	2.255	.3065 ± 0i	N/A
1.5	-1.354 ± 0i	2.954	-.1046 ± 0i	38.241
2	-1.0284 - .2387i	3.890	-1.0284 + .2387i	3.890

2.4.2.3 Vertical Stabilizer

To address the unstable Dutch roll modes, a vertical stabilizer was added to the wing and an additional stability analysis was performed. The longitudinal and lateral modes for the s2046 airfoil are tabulated in Table 13 and Table 14 respectively. Table 13 indicates that the longitudinal stability was not impacted by the addition of the vertical stabilizer. Table 14, however, showed that the Dutch roll instability was eliminated and the Dutch roll settling times were significantly reduced. This analysis, therefore, proved that a vertical stabilizer was an effective solution to maintain lateral stability.

Table 13. Longitudinal Stability Modes for s2046 with Vertical Stabilizer (XFLR5)

Short Period Motion, s2046 Airfoil with Vertical Stabilizer				
Aspect Ratio	Short Period Mode		Settling Time (seconds)	
1	-53.5876 ± 40.0162i		.0746	
1.5	-45.6257 ± 35.4831i		.0877	
2	-40.3202 ± 29.7608i		.0992	
Phugoid Motion, s2046 Airfoil with Vertical Stabilizer				
Aspect Ratio	Phugoid Mode	Settling Time (seconds)	Phugoid Mode	Settling Time (seconds)
1	-2.5364 ± 0i	1.577	1.4804 ± 0i	N/A
1.5	-3.0073 ± 0i	1.330	2.0230 ± 0i	N/A
2	-3.551 ± 0i	1.126	2.5623 ± 0i	N/A

Table 14. Lateral Stability Modes for s2046 with Vertical Stabilizer (XFLR5)

Roll and Spiral Motion, s2046 Airfoil with Vertical Stabilizer				
Aspect Ratio	Roll Mode	Settling Time (seconds)	Spiral Mode	Settling Time (seconds)
1	-2.5512 ± 0i	1.568	1.4723	N/A
1.5	-3.0223 ± 0i	1.323	2.0149	N/A
2	-3.5694 ± 0i	1.121	1.565	N/A
Dutch Roll Motion, s2046 Airfoil with Vertical Stabilizer				
Aspect Ratio	Dutch Roll Mode		Settling Time (seconds)	
1	-50.5782 ± -40.0100i		.0791	
1.5	-45.6147± 35.4777i		.0877	
2	-40.3114 ± 29.7571i		.0992	

3 DETAILED DESIGN AND ANALYSIS

This section discusses elements of the detailed design process following the preliminary design activities outlined in Section 2. A rigorous analysis of the wing's aerodynamic performance was performed using available computational and wind tunnel resources. A detailed design of the fuselage and control surfaces was completed, including placement of components. Trade studies were performed for relevant electronic components including batteries and electric motors. Finally, propulsion hardware was tested to obtain thrust data.

3.1 Aerodynamics

This section discusses the final airfoil selection and detailed aerodynamic analysis of the wing.

3.1.1 Airfoil

The s2027 airfoil was determined to be the best airfoil for our application, as detailed in Section 2.1. Though the s2046 airfoil was determined to be the best airfoil of those considered, it was deemed too thin for foam construction with a thickness-to-chord ratio of only 9%.

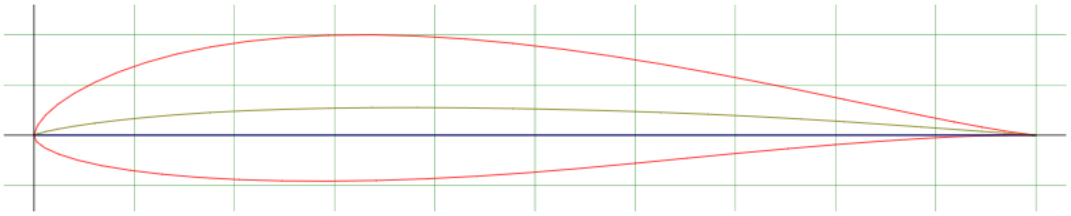

Figure 22. s2027 Airfoil

The s2027 airfoil has a much greater max thickness-to-chord ratio of 14.5%. Based on the aerodynamic analyses of the two airfoils, the difference in aerodynamic performance between the two airfoils is only 3%. The aerodynamic performance is quantified through Eq. 15 and Eq. 16. This airfoil has a stall angle of 12.8 degrees and a max lift-to-drag ratio of 99.7. All the relevant aerodynamic data for the s2027 is listed in Table 15.

Table 15. s2027 Aerodynamic Data

Parameter	Value
C_{l0}	0.300
$C_{l\ max}$	1.40
α_{stall}	12.8
C_{d0}	0.00795
$C_l/C_{d\ max}$	99.6

3.1.2 Planform

It was established in Section 2.2, that the Zimmerman planform would be used. We also determined in Section 2.1 that an aspect ratio of 1.5 and a wingspan of 30 cm would be used. The area was determined using Eq. 13 and can be used in Eq. 22 to determine the length of the root chord. Based on this equation, the root chord c_r will be 25.4 cm. The planform characteristics are given in Table 16.

$$S = \frac{\pi b c_r}{4} \qquad \text{Eq. 22}$$

Table 16. Planform Characteristics

Aspect Ratio	1.5
Wingspan	36.8 cm
Root Chord	25.4 cm
Area	600 cm^2
Mean Aerodynamic Chord	21.6 cm

3.1.3 CFD Modeling

The aerodynamic performance of the wing was evaluated using 3D LES simulations in Ansys Fluent. Ansys Fluent is a popular commercial computational fluid dynamics (CFD) software that solves the Navier-Stokes equations in two and three dimensions. A large control volume was

fitted around the MAV to prevent interactions between the wing and the boundaries of the control volume. Figure 23 details the layout of this domain. This geometry was meshed using ICEM CFD™. Within this program, a mapped hexahedral mesh can be created. To obtain accurate results for the shear stresses and pressures along the MAV, the boundary must be adequately resolved. It is recommended that the first cell centroid should be placed in the viscous sublayer (Moukalled, 2016), which corresponds to a y^+ value of 1 in Eq. 23.

$$y^+ = \frac{d_\perp u_\tau}{\nu}, \quad \text{Eq. 23}$$

where $d_\perp$ is the distance from the wall, ν is the kinematic viscosity of the fluid, and u_τ is the friction velocity given by Eq. 24.

$$u_\tau = \sqrt{\frac{|\tau_w|}{\rho}}. \quad \text{Eq. 24}$$

The shear stress at the wall τ_w is proportional to the Reynolds number Re, and therefore the free-stream flow velocity V_∞ and chord length c through the following relationships described in Eq. 25-Eq. 27.

$$Re = \frac{V_\infty c}{\nu}, \quad \text{Eq. 25}$$

$$C_f = \frac{0.026}{R_e^{1/7}}, \quad \text{Eq. 26}$$

$$\tau_w = \frac{1}{2}\rho V_\infty^2 C_f. \quad \text{Eq. 27}$$

C_f is the skin friction coefficient. To achieve a y^+ value of 1, the first layer thickness had to be approximately 10^{-5} m thick. A series of subsequent layers of cells were created around the wing to adequately resolve the boundary layer. The resulting mesh had approximately 15 million cells. The domain was partitioned into 16 subdomains to be solved using computational resources supported

by the Academic & Research Computing group at WPI. The velocity-inlet boundary condition was used for the domain inlet. Velocity inlets are used to define the velocity and scalar properties of the flow entering the domain (ANSYS, 2009). The $\hat{\imath}$, $\hat{\jmath}$ and $\hat{k}$ components of the inlet velocity unit vector can also be defined. The $\hat{\imath}$ and $\hat{\jmath}$ components of the velocity represent the typical horizontal and vertical components of airspeed. These components can be manipulated to achieve a desired angle of attack with respect to the wing. The $\hat{k}$ component represents the velocity in the spanwise direction of the wing and is neglected. An outflow boundary condition was used for the flow outlet. An outflow boundary condition stipulates that there is a zero diffusive flux for each flow variable (ANSYS, 2009). The surface of the wing was defined as a no-slip wall. The top, bottom, and sides of the domain were defined as symmetries, with a zero diffusive flux condition.

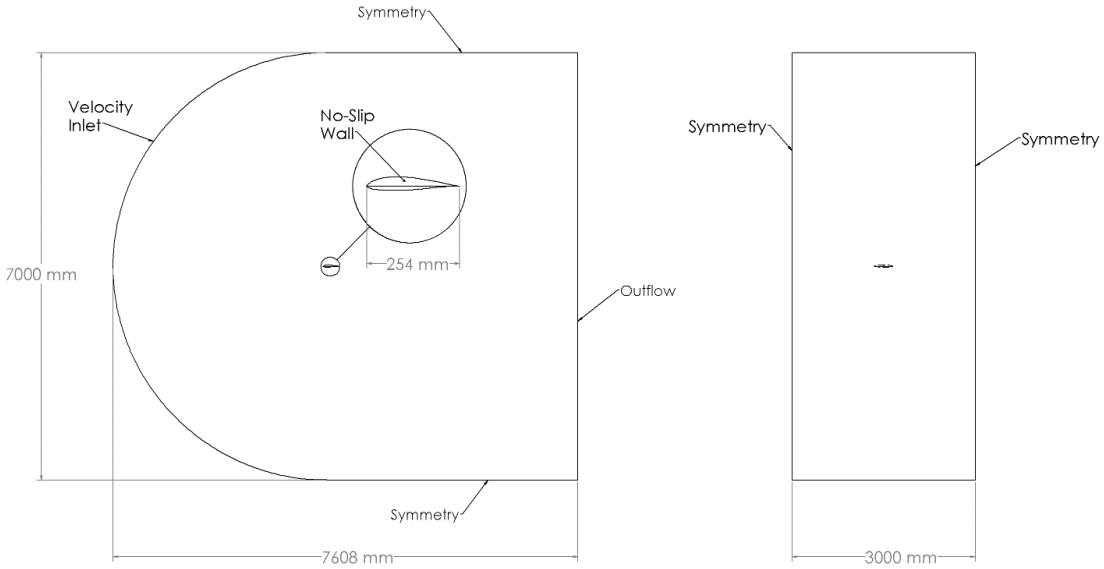

Figure 23. CFD Domain Schematic

To obtain a solution, a velocity field was first generated using a simple steady-state laminar flow model until the velocity field around the wing was partially developed. A transient LES simulation with the Smagorinsky model was then initialized and run until the flow covered a full-

length scale of the domain. Finally, force monitors on the wing were initialized and the LES model was run further to obtain lift and drag data. A characteristic time scale can be defined using the root chord of the wing and the freestream velocity. Dividing the root chord length by the flow velocity (18 m/s) gives an approximate timescale of 0.01 seconds. The data was sampled for 0.1 seconds, which corresponds to 10 times the characteristic time scale, with a sampling frequency of 10 kHz. Figure 24 is an example of the fluctuations in the lift force as a function of time; the time averages of the lift and drag forces were used to calculate the lift and drag coefficients. Figure 25 shows how the results from the LES simulations compare with those from XFLR5 under the same conditions. The same grid was used for each LES simulation. There was not enough time to try a different grid with different types of cells (i.e. tetrahedra, polyhexcore, etc.).

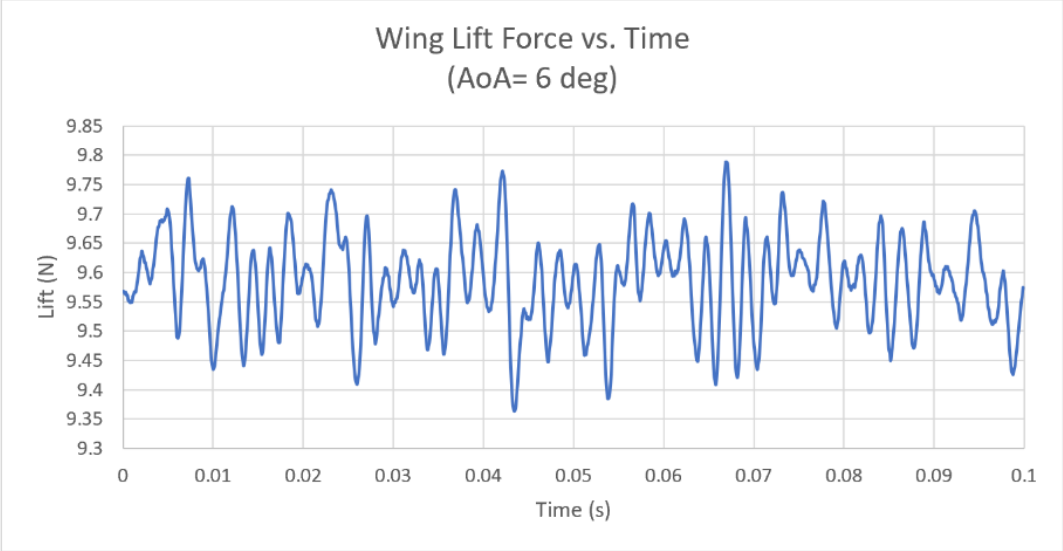

Figure 24. Lift Force Fluctuations

(a) (b)

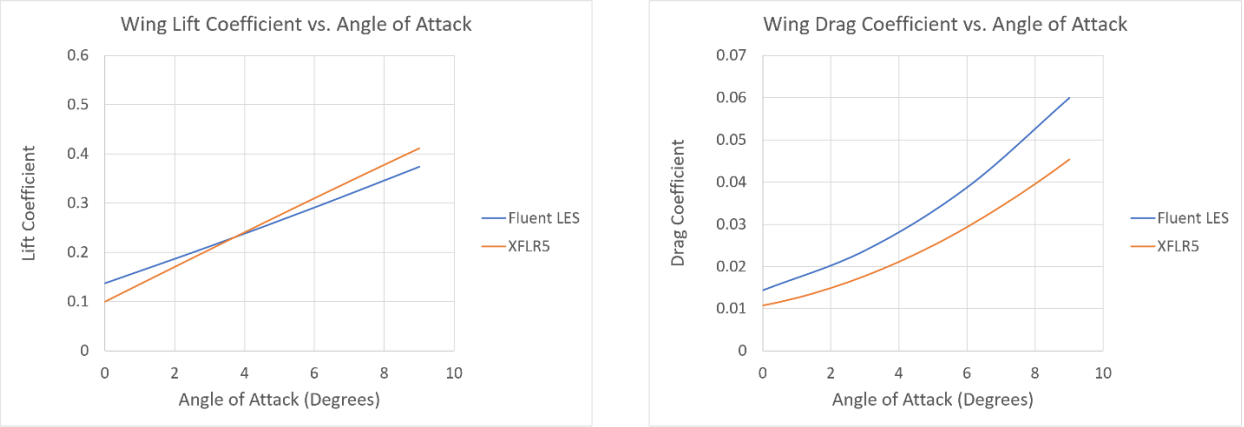

Figure 25. (a) Lift & (b) Drag Coefficient vs. Angle of Attack

As the angle of attack increases, the solver begins to become unstable. This is evidenced by a sudden divergence in the mass and momentum conservation residuals. Residuals are scaled differences between the outputs of two subsequent iterations of the numerical solver and are an indication of the solution's accuracy. The residuals are printed after each iteration to allow the user to monitor the solver. Several factors can lead to instability and divergence. The first factor is poor cell orthogonality, which can be problematic in regions in the flow where there are large gradients, such as around the wing. Such cells are created around the wingtips due to the Zimmerman wing shape. Fluent can cope with cell non-orthogonality to a limited degree by reducing under-relaxation factors (ANSYS, 2009).

Fluid solvers, such as OpenFOAM, treat cells with poor orthogonality differently by splitting the normal vector between neighboring cells into orthogonal and non-orthogonal components (Jasak, 1996). The orthogonal component can be solved implicitly, thereby increasing stability. The non-orthogonal component is solved explicitly, which decreases stability. Having cells with good orthogonality will keep the contribution of the explicit term small compared to the

implicit term. If the contribution of the explicit term is too large, then OpenFOAM will limit its contribution by a factor less than 1 to force a more stable solution (Jasak, 1996).

Another factor that has led to the divergence of our solutions is the outlet boundary condition. Specifically, we are facing issues with reversed flow at the outlet, according to error messages from Fluent. Presently, the specific cause of this error is unknown. One such cause could be vortex shedding which occurs at higher angles of attack. One possible way to fix this is to extend the length of the domain behind the wing more to allow the turbulence to dissipate before reaching the outlet.

3.1.4 Wind Tunnel Testing

WPI's wind tunnel was used to further test the wing and validate the results from the CFD and XFLR5 simulations. A 3D-printed mount was created to mount the wing to the force balance. The force balance consists of a four-bar linkage that can be used to adjust the angle of attack relative to the flow. The force balance rests on top of a scale that can be used to measure the lift in grams. A freestream velocity of 18 m/s was used, and the wing was tested at different angles of attack ranging from -10 to 18 degrees in 2-degree increments. Prior to fixturing the wing, the mount was tested to determine its contribution to the overall lift. This was followed by four subsequent runs with the wing attached. The results were averaged at each angle of attack between the four runs, and the standard deviations were calculated. Figure 26 shows the averaged lift curve.

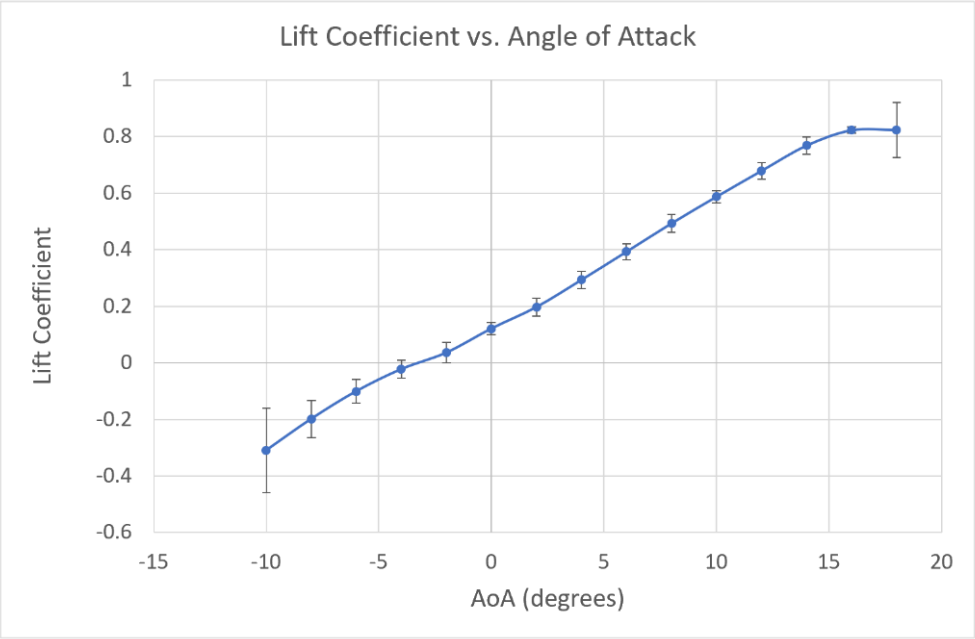

Figure 26. Wind Tunnel Lift Curve

The plot shows that the uncertainty grows at the lowest and highest angle of attack. This is due to the oscillations induced by flow separation which lead to fluctuations in the scale's readout. The uncertainty at the highest angle of attack is also due to the increased drag which often pushed the force balance backward. There was not sufficient time to test the wind tunnel using a control, such as a well-documented NACA airfoil. Thus, the effects of the experimental setup on the measurements are not fully understood. At lower angles of attack, the results from the simulations show good agreement with the wind tunnel results but diverge as the angle of attack increases (Figure 27). Using the wind tunnel data, the stall angle was determined to be approximately 17 degrees, with a maximum lift coefficient of approximately 0.82.

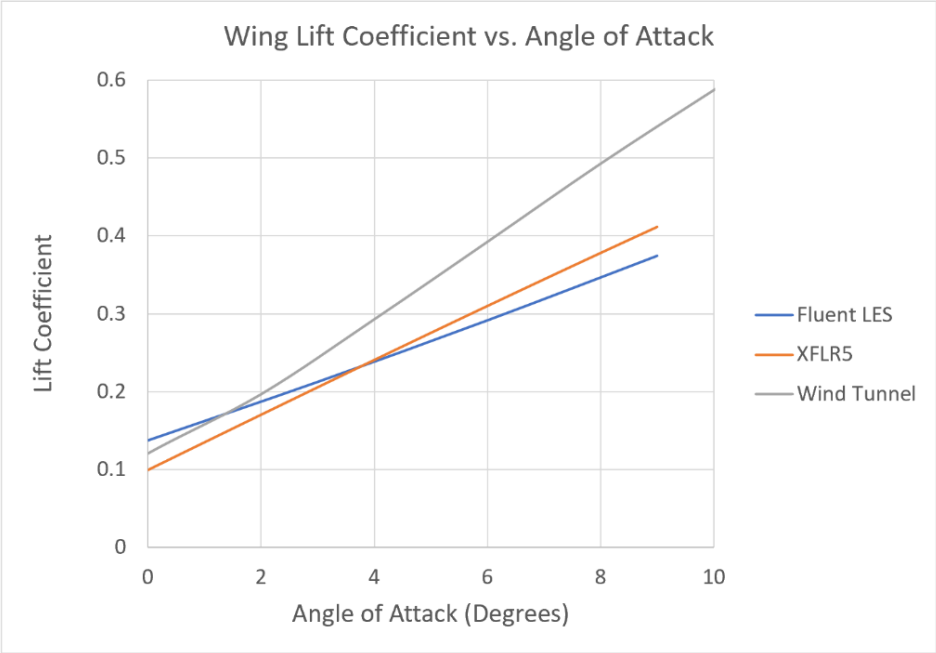

Figure 27. Lift Coefficient vs. Angle of Attack

3.2 Fuselage

The team further refined the fuselage shape from initial models into one that can fit the payload inside and has less boundary layer separation towards the back of the fuselage, this design can be seen in Figure 28. Boundary layer separation in external flows is caused by an adverse pressure gradient that can cause the flow in the boundary layer to slow until the flow near the wall begins to reverse direction. This reversal of flow creates a local stagnation point at which point the flow will separate from the wall (Kundu, 2016). Streamlining the fuselage to make the curvature more gradual can allow the flow to stay attached for longer. The new design has a more cylindrical shape, reflective of larger transport aircraft and high-speed jets. It also has a nose cone dedicated to the motor housing. The top of the fuselage is curved along the airfoil paths to allow it to fit snugly to the bottom of the wing. This means no cuts needed to be taken from the front of the wing to interface with the fuselage. The front clip was kept, easing the attaching of the fuselage to the

airfoil. The rounded cone also meant that the clip interrupted much less of the leading edge of the wing than the clip seen in the first theoretical model, previously shown in Figure 18. One problem with this design is it requires tight curves out of the balsa wood, which may cause the wood to snap during construction. To mitigate this, we chose to instead build the fuselage out of foam in the same manner as the wing.

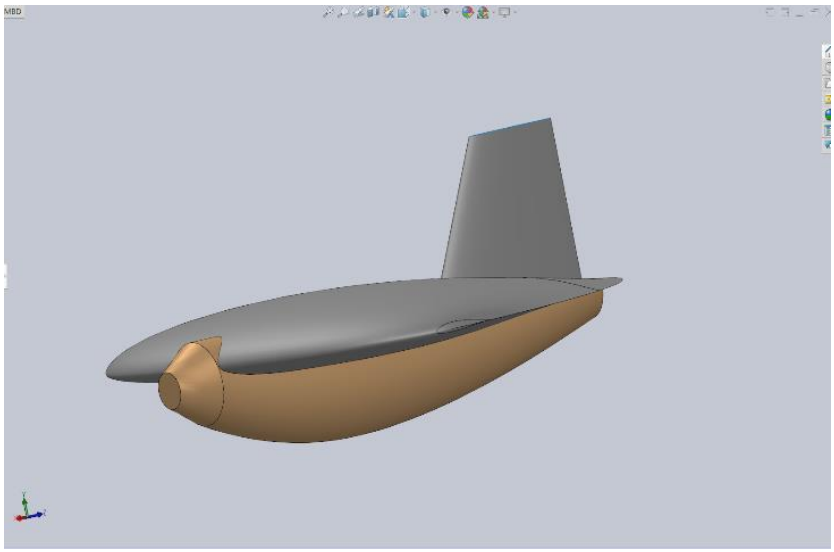

Figure 28. Detailed Fuselage Design

This fuselage version was modeled along with the corresponding wing using auto-generation of airfoils. A MATLAB script was created to generate 200 airfoils along the length of the span, and then a SolidWorks macro was created to put the curves into SolidWorks and form the wing. The same airfoil coordinates were used to create the matching curve on the fuselage and connect the wing to the tail. As shown in Figure 29, some of the components cut into the wing and the tail, which required cuts to be taken from them to allow the components to be placed inside. Since these areas are inside the fuselage and do not break the top surface of the wing, the airflow over the top of the wing will not be disturbed.

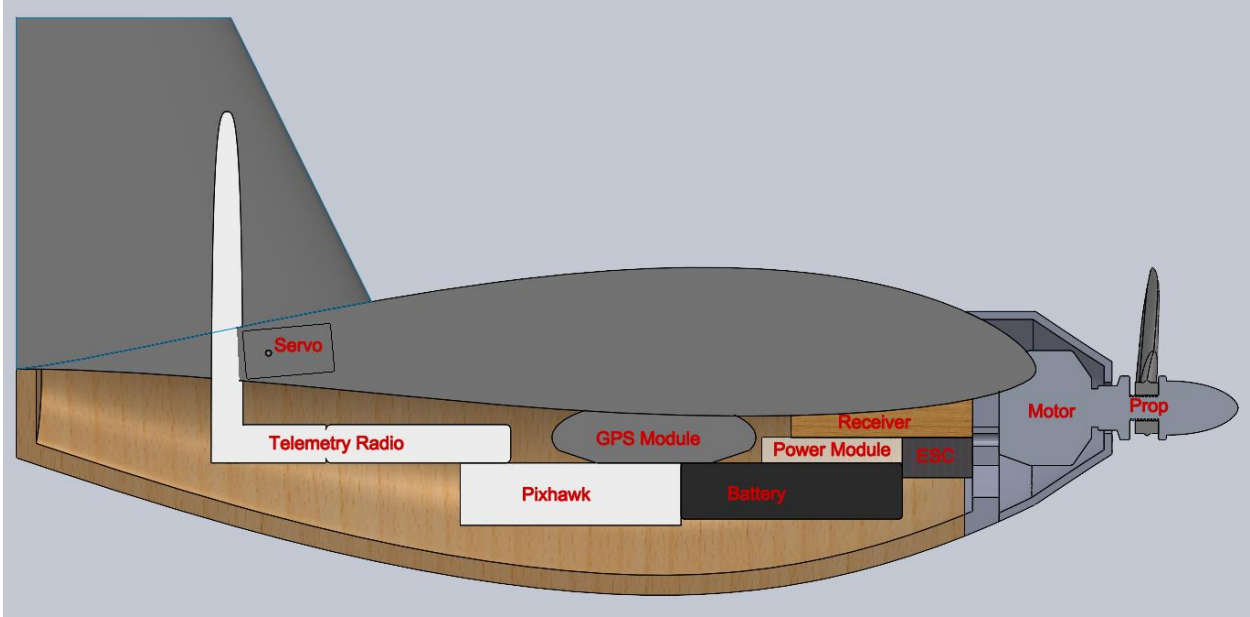

Figure 29. Inside of Fuselage

The nose cone was also separated from the fuselage itself since the foam would not provide enough stability or heat resistance for the motor compartment. The nose cone was separated into two pieces for motor insertion and was 3D printed using PLA. The front is the actual cone (see Figure 30a), and the back consists of the mount with a hole for the motor wires to go through (Figure 30b). The nose cone is then assembled with the motor and propeller as seen in Figure 31.

(a) (b)

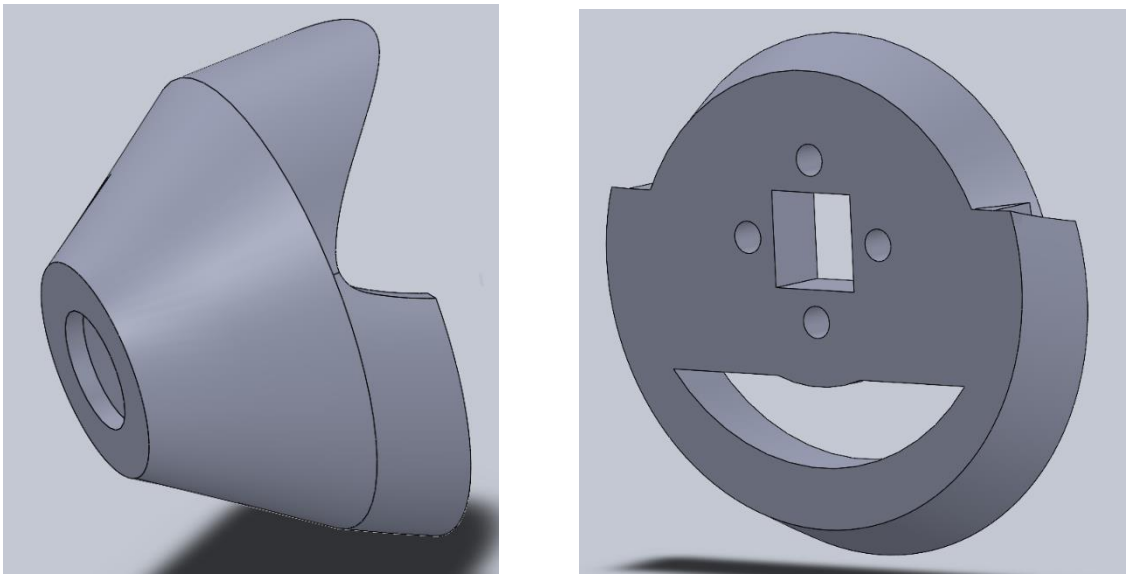

Figure 30. Nose Cone Front and Back

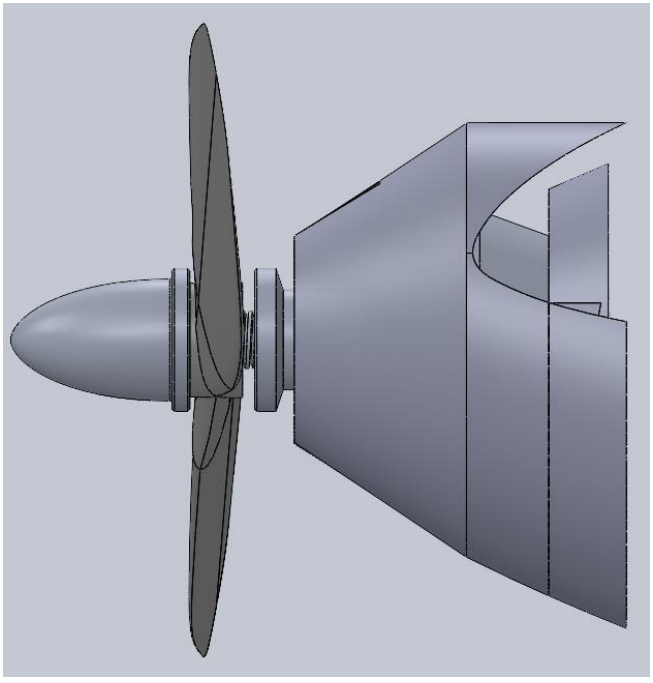

Figure 31. Assembled Nose Cone

To account for this separation of the nose cone, the front of the fuselage was removed to make room. Figure 32 and Figure 33 show the fuselage without and with the nose cone, respectively.

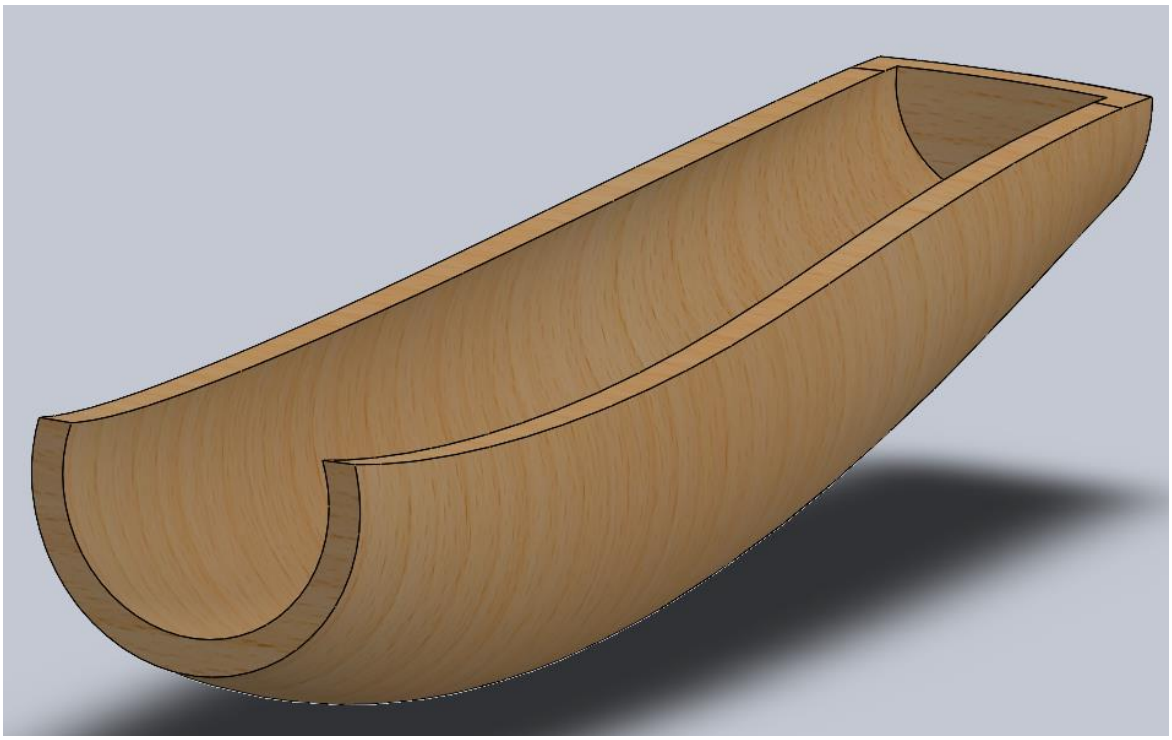

Figure 32. Fuselage Without Nose Cone

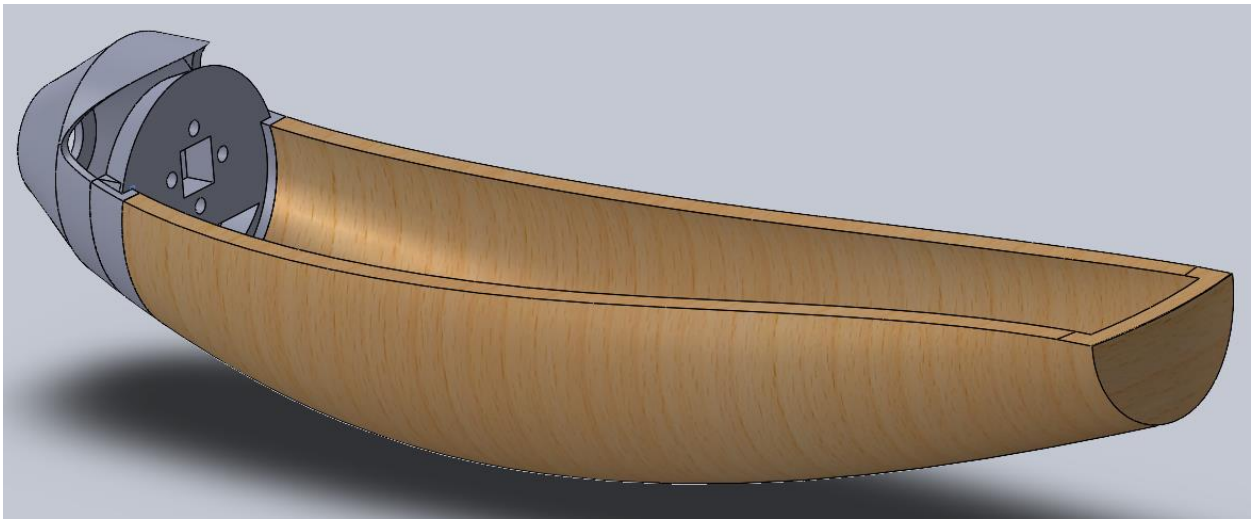

Figure 33. Fuselage Design with Nose Cone

3.3 Control

This section discusses the detailed design and integration of the control surfaces, as well as the flight controller.

3.3.1 Control Surfaces

Control surfaces are critical to aircraft motion, and the stability team came up with two options for the movement of the control surfaces. The simplest design is to connect the servos directly to the control surfaces through a rod that runs through the control surface. The other option is with a push rod and a control horn cut into the control surface. The servo moves the pushrod which moves the control horn and thus the control surface (Federal Aviation Administration, 2016).

The combination of the push rod and control horn is a more efficient option than the direct connection to the control surface. Moving a rod within the control surface requires greater torque than the control horn since there is less leverage. The control horn typically involves splitting the control surface in two and placing the control horn in between the sections. While the control horn is a good option for larger MAV models, we found that the fuselage design and size of the wing did not allow for the room required to move control surfaces in this manner. To test the idea of putting the push rod directly into the elevons, a SolidWorks motion study was completed which included gravity and frictional forces. This study was found to give a range of motion in the elevons of approximately 90 degrees: 45 degrees above and below the yaw plane.

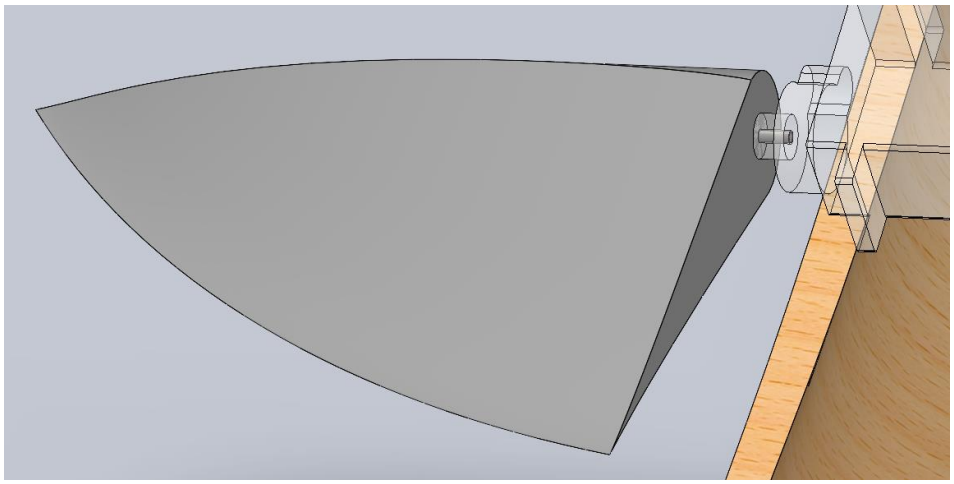

Figure 34. Control Surface Push Rod

As can be seen from Figure 34 the push rod connects directly to the center of the elevon. The end inside the fuselage is connected to the servo (seen in the figure as transparent), with the bend removed from the push rod so the servo is directly on the axis of rotation. Figure 35 shows the two elevons deflected in opposite directions using the direct servo push rod method.

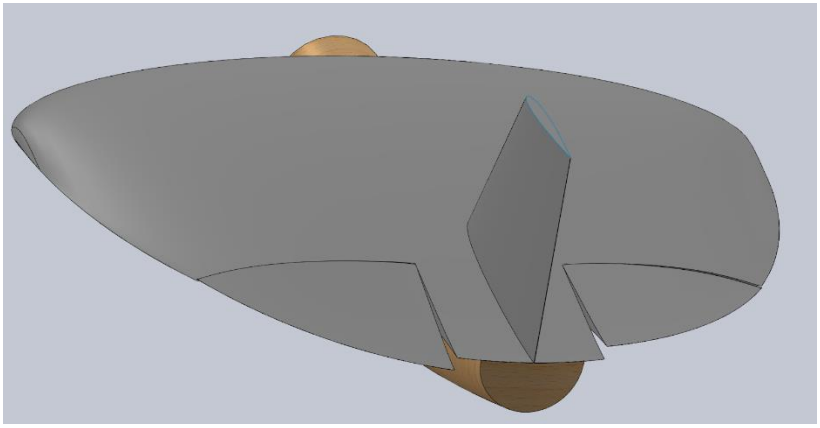

Figure 35. Deflected Control Surfaces

3.3.2 Flight Controller

After doing some research into different flight controllers, the team decided to go with the Pixhawk 4 mini. The Pixhawk 4 Mini is a small and compact processor weighing only 37.2 grams with dimensions of 38 x 55 x 15.5mm. This is ideal for our aircraft because it is lightweight, and

the size allows for easy attachment. The Pixhawk also has four useful onboard sensors that are needed to analyze the overall flight attitude. The controller has two accelerometers/gyroscopic sensors, a magnetometer, and a barometer. The two accelerometers and gyroscopic sensors help acquire the inertial measurements of our aircraft and having two sensors account for redundancy. To extract the flight data from the Pixhawk, the team will be using QGroundControl due to its easy-to-use interface and ability to save the data logs after each flight. These logs can be loaded into MATLAB's Flight Log Analyzer which plots the flight attitude data, accelerometer data, and gyroscopic data. This helps in being able to visualize the flight of the MAV and address potential stability issues.

3.4 Electronics

Due to their small size, MAVs require small electronic components to both fit within the fuselage and not increase the mass significantly. Thus, electronic components were chosen to minimize weight and dimensions. A summary of the electronics components considered is shown in Table 17. This table does not include motor options or their corresponding ESCs. The micro-receiver and servos were chosen for their small size and low cost. The micro-receiver also needed to be compatible with the Spektrum DX8 transmitter provided by WPI. The batteries offer a range of discharge rates and sizes for the maximum storage capacity of 1000mAh. The motor selection with govern the choice of the battery.

Table 17. Electronic Components Considered

Component	**Weight**	**Dimensions**
Spektrum AR410 DSMX 4-Channel Sport Receiver	7 g	45x20x14 mm
SG90 Micro-Servos	18 g (for two)	N/A
Turnigy 11.1V 1000mAh 3S Li-Po Battery	108 g	77x20x33 mm
Lumenier 11.1V 1000mAh 3S Li-Po Battery	81 g	70x35x18 mm
Blomilky 7.4V 1000mAh 2S Li-Po Battery	45 g	55x30x14 mm
Urgenex 7.4V 1000mAh 2S Li-Po Battery	51 g	54x30x16 mm

Three DC motors with different power outputs were considered; all three are produced by E-Flite. The motors can power aircrafts with weights in the range of 115-560 g. These motors will provide adequate power for any MAV the team designs. The motor specifications are listed in Table 18.

Table 18. Motor and ESC Specifications

Motor	**Weight**	**Sizing**	**Diameter**	**Power/Voltage**	**ESC**
Park 250 2200kV Brushless	14 g	115-340 g Aircraft	20 mm	55 W/7.4 V	E-Flite 10A Pro ESC
Park 370 1360kV Brushless	45 g	200-400 g Aircraft	28 mm	150 W/7.4-11.1 V	E-Flite 10A Pro ESC

Park 400 740kV Brushless	56 g	280-560 g Aircraft	32 mm	N/A W/7.4-11.1 V	GraysonHobby 18A ESC

The total weight of the aircraft was estimated based on two choices of chord length: 8 in and 12 in. These lengths were chosen as a range of the possible smallest and largest aircraft we would create. The wing and fuselage were both scaled to fit these chord lengths but shared the same design. Weight changes between the two based on motor and battery selection is shown in Table 19. The 12 in chord design is compatible with both options of motor and battery; the heavier of which would be more favorable for a larger structure. According to the E-Flite Power Requirement Manual (Appendix 1: E-Flite Model Power Requirements), these Power-to-weight ratios provide enough power for advanced and sport aerobatic model aircraft.

Table 19: Electronic Options for Differing MAV Sizing

Chord length	8 in	12 in	
Total Weight (g)	194	240	304
Motor	Park 250	Park 250	Park 370
Battery	Blomilky 7.4V 1000mAh 2S Li-Po Battery	Blomilky 7.4V 1000mAh 2S Li-Po Battery	Lumenier 11.1V 1000mAh 3S Li-Po Battery
Power-to-weight ratio (W/lb)	127	103	221

3.5 Propulsion

The propulsion system of the aircraft is driven by the motor and propeller. Physical testing of static thrust was completed in the lab using a force balance. Different combinations of

motors, batteries, and propellers were analyzed until finding a set that would generate adequate thrust.

3.5.1 Static Thrust

Static thrust tests were performed on the motor using a mount with a long lever arm attached to a scale. The motor was attached to the long arm, and the short arm was placed above the scale (Figure 37). The premise behind this is that the force produced by the motor is magnified on the end with the scale due to moment balancing. The long and short lever arm measured 47 inches and 11.5 inches in length, respectively. In Figure 36, the green arm represents the short lever and the red the long. This resulted in a magnification of the thrust by a factor of 47/11.5—or ~4.09X.

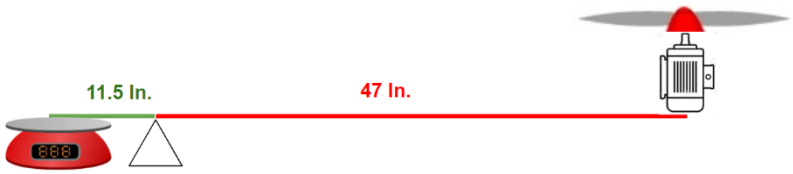

Figure 36. Static Thrust Testing Diagram

Figure 37. Annotated Static Thrust Testing Setup.

The motor was controlled by an Arduino since we did not have access to a micro-receiver compatible with our controller at the time. In the circuit, as shown in Motor Testing Setup, the Arduino provided a potentiometer-controlled voltage signal to the ESC. The ESC was connected to the battery and motor as normal. The potentiometer acted as a replacement receiver, where turning the wiper provides an analogous effect to throttling up and down. The main problem with this setup was the throttle determined by the potentiometer could only be set once before throttling back down to zero and resetting. Any throttle setting besides full throttle was imprecise since there was no way to determine what angle the wiper was at when the motor turned on. Thus, the motor was only tested at full throttle. The scale averaged 1250 g at full throttle, which indicates an average thrust at full throttle of 306 g (~3N).

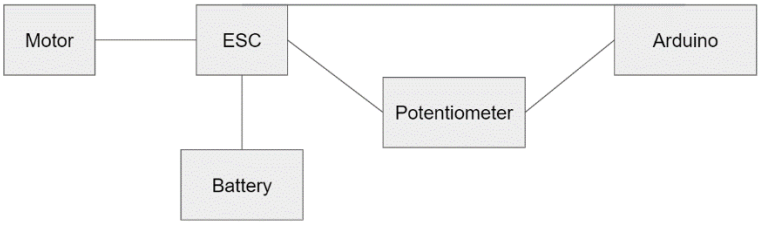

Figure 38. Motor Testing Setup

3.5.2 Dynamic Thrust

To generate theoretical thrust values for different motor, battery, and propeller configurations, a Dynamic Thrust Equation (Eq. 28) was used. This equation was derived by Gabriel Staples from a theoretical mass flow through the propeller given prop velocity (RPM_{prop}), pitch, and diameter d (Staples 2014). Since a propeller cannot accelerate airflow past a certain point, the flow velocity V_0 is multiplied by the second mass flow term. If V_0 is large enough, the thrust of any propeller configuration tends to 0 (Staples 2014). These different motor/battery configurations were graphed in Figure 39 in the following pairs according to Eq. 28 to select the best combination for the requirements of the MAV. The dashed lines correspond to the motors paired with the Lumenier battery, and the solid lines correspond to pairings with the Blomilky. As explained before, it can be seen from the Park 370 (red) that by pairing it with the Lumenier battery (red dashed) that even at a velocity of 20 m/s results in considerable thrust whereas the Blomilky (red solid) thrust would be close to 0.

$$F = 1.225\frac{\pi(0.0254 * d)^2}{4}\left(\left(RPM_{prop} * 0.0254 * pitch * \frac{1\ min}{60\ sec}\right)^2 - \left(RPM_{prop} * 0.0254 * pitch * \frac{1\ min}{60\ sec}\right) * V_0\right) * \left(\frac{d}{3.29546\ *\ pitch}\right)^{1.5}$$

Eq. 28

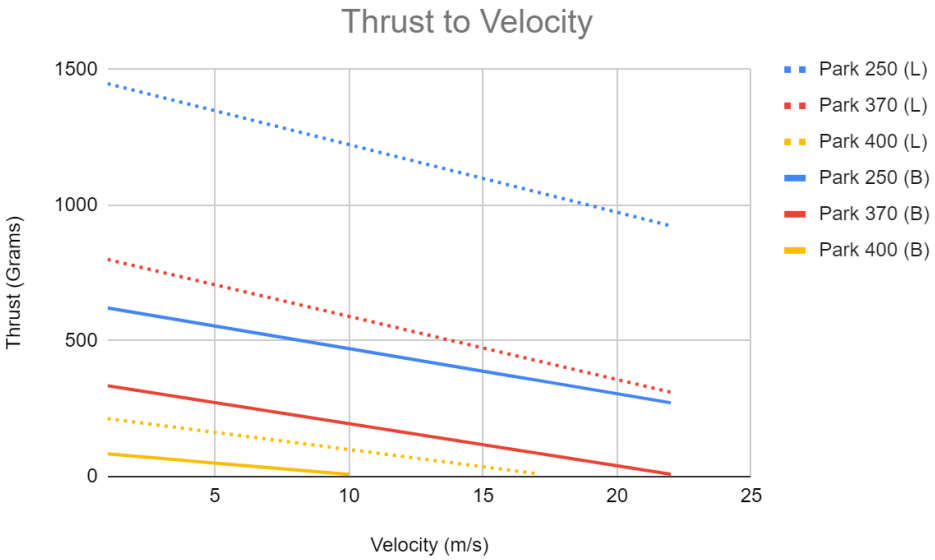

Figure 39. Dynamic Thrust as a Function of Velocity

4 FINAL DESIGN MODIFICATIONS

Areas for improvement were identified following the construction and testing of the detailed design discussed in Section 3. This section discusses the modifications developed to achieve the final design.

4.1 Fuselage

While the preliminary fuselage was able to fit all the necessary components, the shape and size proved to be restrictive. The rounded shape prevented the large rectangular battery, Pixhawk, and payload from sitting well into the fuselage leaving considerable gaps and spaces. Additionally, the gauge of the wires for certain components were larger than expected; these were not considered during initial design for fuselage sizing and weight calculations. As a result, some of the components were forced further back in the aircraft to get everything to fit securely even after removing material from the bottom of the wing. After assembling the full preliminary MAV, a simple balance test was conducted. The center of gravity was close to the center of the aircraft which was well behind where the preliminary weight analysis suggested. A rough attempt at a lasso test made it clear that this balance offset invalidated initial longitudinal stability calculations. An analysis of this test is found in Section 6.1. To combat this issue, heavier components needed to be more forward in the fuselage—which was not possible due to the lack of space. Additionally, the components were not secure in the rounded shape. To solve both problems, a flat-bottomed fuselage was designed. The revised version was also lengthened to ensure space for various wires and allow for freedom to move components forwards or backwards if necessary. The nose cone was kept the same as it housed the motor securely and safely.

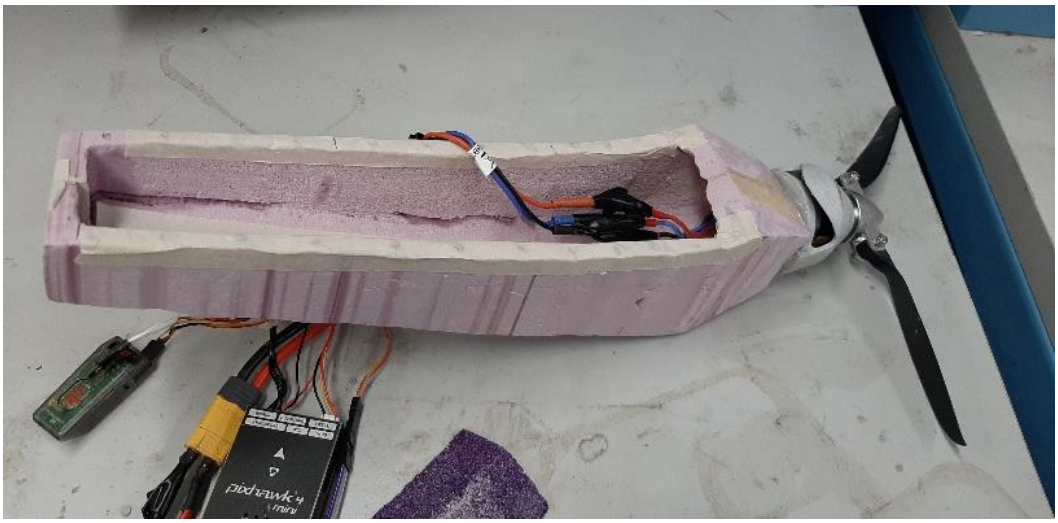

Figure 40. Final Fuselage Iteration

The final fuselage is shown in Figure 40. To keep the fuselage secured to the wing, a set of 24 magnets was imbedded around the perimeter of the fuselage/wing interface. Another set of magnets was secured to the wing to allow the fuselage to be snapped on and off easily, allowing for access to the internal components between tests.

4.2 Wing

When we increased the length of the fuselage for the final design, the maximum length of the aircraft increased. As a result, the wingspan was no longer the limiting factor for the size portion of the scoring equation. In other words, the wingspan could be increased without impacting the score. The Zimmerman shape with the same chord length was kept for the final design but the wingspan was scaled up about 27.5% as seen in Figure 41; the result was a wingspan of 36.8 cm. One of the benefits of this is that the increased lift would help offset the weight increase of the fuselage. Additionally, a higher aspect ratio wing would increase the lateral stability of the aircraft.

Figure 41. Wing and Wing with 27.5% Increased Wingspan

4.3 Control Surfaces

Testing revealed inputs from the controller had insignificant effects on the flight of the preliminary model; more on testing found in Section 6.

Additionally, the elevons only connected to the wing through the straightened pushrods and servo arms directly fixed to the servos. Under light loads and unresisted rotations, the elevons were bending in unintended directions and not rotating along a consistent axis. To fix the first issue, the elevons were enlarged for the final design; in turn, this amplified the bending. A new way to support the elevons was needed. Control rods were used as simple pivots, fixed to the wing itself and fed into the far edge of the elevon from the servo as seen in Figure 42. This structure kept the elevons in place without limiting rotation.

Figure 42. Control Rods Inserted in Elevon

4.4 Electronics

Based on the thrust testing, the Park 370 was chosen as our final motor. This motor used the E-Flite Pro Brushless ESC which was compatible with the micro-receiver and servos mentioned in Section 3.4. During testing, we used the Blomilky battery in hopes of reducing the battery weight.

The arming plug required soldering of the battery with the power distribution board (PDB) of the Pixhawk, which used bullet connectors. The Blomilky used JST connectors that were not compatible with the PDB, therefore the Lumenier battery was used instead. While this battery increased the total weight by 36g, it allowed for easier connections between the battery, arming plug, and PDB.

5 FABRICATION AND CONSTRUCTION

This section discusses the fabrication and assembly of the detailed and final MAV designs. The evolution of the manufacturing process is presented, as well as relevant safety and procedural considerations.

5.1 Initial Steps

Polystyrene foam models can be created using a foam cutter for the initial shaping. Some model builders use drawn-on stencils as guides for the cuts and others try to shape their models mostly by careful estimation and experience. Due to its high strength, the densest available polystyrene foam, *Foamular 1000*, was used. Given the limited experience our group has with foam construction and the research completed on exact shapes for the airfoil and planform, a new manufacturing process to increase precision was needed. This process consisted of laser cutting balsa wood guides for slices of the wing at even intervals across the wingspan. The foam was sandwiched between the balsa wood slices, which were aligned using a stiff wire or dowel, resulting in rigid cutting guides. This process ensured both symmetry across the wing and a smooth and strict adherence to the selected airfoil shape. More details and pictures of this process can be found in Section 5.2.

5.1.1 Tools and Material

The materials used in wing fabrication:

- Balsa wood
- Polystyrene Foam
- Gorilla Glue
- Wooden Dowels
- Magnets

The tools used in the wing fabrication:

- Laser cutting machine
- Hot-wire foam cutter
- Electric Drill
- Large Clamps
- Paintbrush
- Assorted Files
- Sandpaper

The materials used in fuselage fabrication:

- Balsa wood
- Polystyrene Foam
- Gorilla Glue
- Wooden Dowels
- PLA Filament
- Magnets

The tools used in the fuselage fabrication:

- Laser cutting machine
- Hot-wire foam cutter
- Electric Drill
- Large Clamp
- Paintbrush
- Sandpaper
- 3D Printer

5.1.2 Lab procedures and safety

Given the rise of COVID-19 cases amidst our lab work in B-term, COVID safety was the number one concern. As a result, lab-work strictly adhered to all guidelines set by both the State of Massachusetts and WPI. Regardless of the number of individuals in the lab, masks were always worn, and surfaces were disinfected before and after use. If team members were required to work together in proximity that exceeded social distancing requirements, face shields were worn.

For wing fabrication, the only power tools required were the hot-wire foam cutter and the electric drill. Primary concerns included ensuring proper eye protection while the drill was in use and keeping all body parts and extremities away from the drill bits, wire of the foam cutter, and any other sharp or hot edges. Standard lab procedures applied including no open-toe footwear, gloves when handling equipment, long hair tied up, etc.

Additional lab safety included LiPo battery safety, which required unique procedures for proper usage. For example, new batteries had to be "broken in" by charging and discharging through 6 or 7 cycles before operating under real loads. This had to be completed under specific conditions of only 1 Ampere. The batteries were discharged to a minimum of 3.5 Volts and charged to a maximum of 4.2 Volts. Most modern LiPo battery chargers have indicators when this occurs and some even have built-in break-in cycle programs. The performance and lifetime of LiPo batteries are dramatically affected by the way they are broken in and maintained thereafter. Additionally, batteries must always be charged and discharged inside a battery-safe box with someone always attending. They must never be charged over 4.2 Volts per cell or less than 3.0 Volts per cell. LiPo batteries must also be stored at a storage charge of 3.8 Volts per cell (34% charge) for both short- and long-term storage.

5.2 Fabrication

This section details the wing and fuselage fabrication process, including initial and refined techniques. Assembly of the fabricated components is also presented.

5.2.1 Wing

Fabrication was initially completed on the wing from the detailed design. The first step in the wing fabrication process was to cut out the rectangular pieces. Figure 43 shows the fixture that was set up to ensure even, smooth cuts. 2D slices of our wing, which were created from the 3D CAD model, were used to laser cut 1/32-inch balsa wood slices. These were aligned with each other and two holes were drilled into them. These slices were then arranged between the foam slices and a stiff wire was run through the whole assembly to align all the pieces as shown in Figure 44. Following the alignment, Gorilla Glue was applied to each piece and everything was clamped together and allowed to cure for 24 hours, as shown in Figure 45.

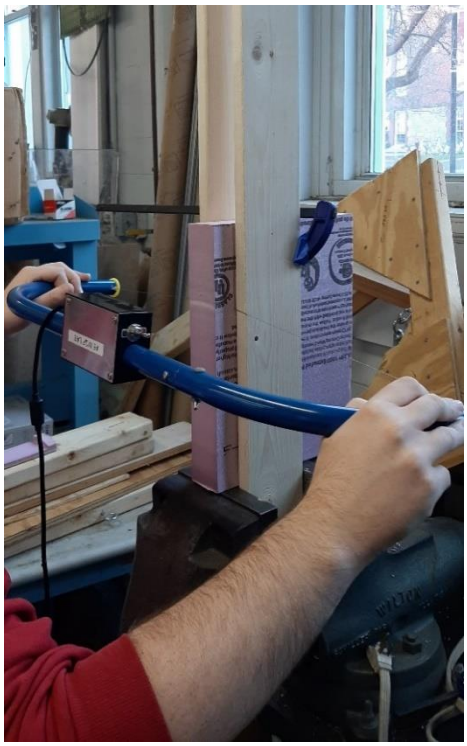

Figure 43. Cutting the Basic Pieces

Figure 44. Aligning Spars and Foam

Figure 45. Glue Curing Setup

Once the glue was fully cured, the stiff wires were removed, and the shaping of the wing began. The hot wire foam cutter was used to obtain the rough shape of the overall wing. If the

pressure was kept light on the cutter, the wire would glide over the wooden spars and create smooth cuts as shown in Figure 46. The wing was then sanded down with coarse files, followed by a finer sandpaper to bring it close to its final wing shape seen in Figure 47. Though the wing was rougher than initially intended, it served as an adequate proof of concept for the fabrication process.

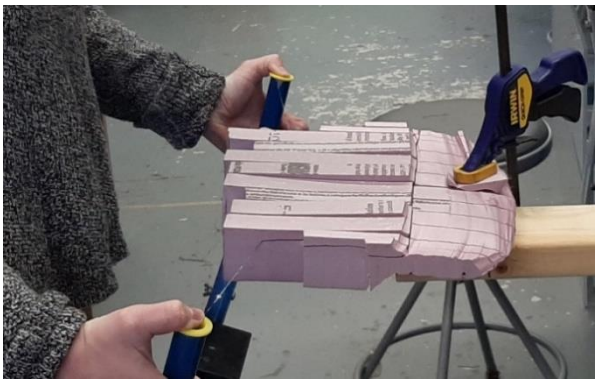

Figure 46. Foam Cutting the Wing Shape

Figure 47. The Sanded Wing

Achieving a smooth surface across the wooden spars with additionally sanding proved difficult, as the foam sanded away much quicker than the wood. A second prototype was fabricated with a greater number of slices. The number of slices was increased such that each slice was 0.3 inches thick. Additionally, the balsa wood spars were not glued to the foam, only used as guides for the wire cutter. The same assembly and gluing processes were maintained. The all-foam result greatly improved the profile of the wing even before sanding (Figure 48). Likewise, the sanding

process resulted in an improved surface finish. Lastly, rear portions were cut from the back of the wing to be replaced by the elevons, as shown by the 90-degree cuts in assembled wing pictured in Figure 49. The same fabrication technique was applied to the final design wing. The only difference between the final wing and the previous prototypes was the thickness of the initial foam slices, increased from 0.3 to 0.375 inches for the larger wingspan.

Figure 48. Final Wing Before Sanding.

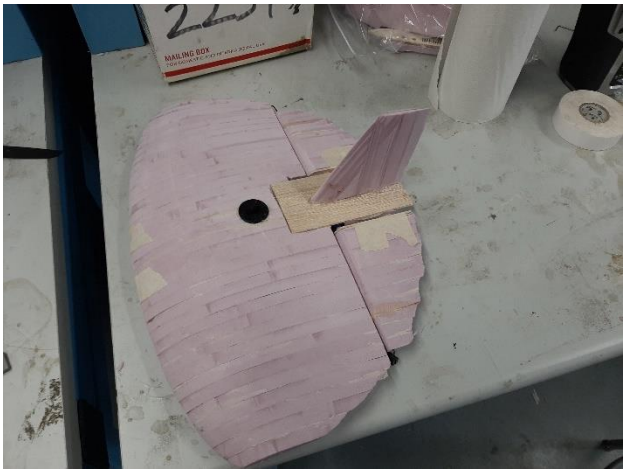

Figure 49. Assembled Final Wing.

5.2.2 Fuselage

Following the successful wing creation using slices, the same process was followed with the fuselage using 0.75” thick slices. Problems were encountered during this build process that

were not experienced during the wing construction. To include a dowel hole that could align all the pieces of the fuselage, the guides had to be extended beyond just the slices in the 3D Model. The result was that the inner curve of the body was just a narrow slit on the guides and in our first attempt at laser cutting them, the wood was not cut all the way through. A group of the fuselage guides is shown in Figure 50.

Figure 50. Fuselage Balsa Guides

After cutting new guides, the narrowness of the slits continued to slow down the build process as the hot wire cutter would occasionally be caught on the wood and could destroy the piece as it was being pulled free. The assembled slices of the preliminary fuselage can be seen in Figure 51.

Figure 51. Foam fuselage.

The nose cone required a different approach for a few different reasons. Firstly, the complexity and size of the cone would make it difficult to manufacture using the same method as the rest of the fuselage. Second, the location of center of gravity in SolidWorks indicated that more weight in the front of the aircraft may be needed to obtain static stability. Finally, there were concerns regarding the motor and the foam. Creating a rigid mounting point for the motor using foam would be unlikely. Furthermore, the temperature of the motor during operation can reach up to 220°F, which caused concerns about its proximity to the foam. The nose cone and engine mount, therefore, were 3D printed with PLA filament and glued to the rest of the fuselage after the motor mounting and assembly were complete. The two can be seen mounted together in Figure 52.

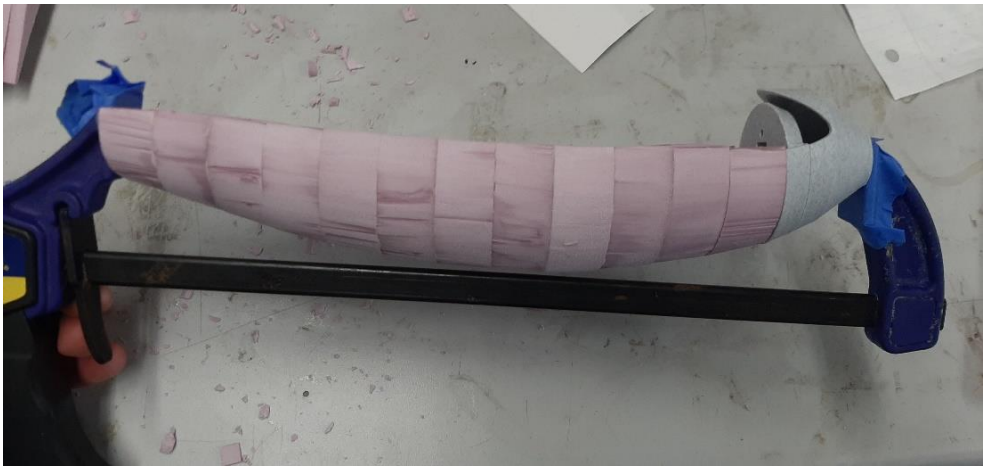

Figure 52. Foam wing with 3D printed nose cone.

Fabrication of the final fuselage was greatly simplified. Only two pieces of foam were joined down the center of the fuselage. A side and top template were created for each side on standard printer paper. After the blocks were cut and sanded smooth, the internal material was removed to achieve the desired wall thickness of ¼". Figure 53 shows the side view of the final fuselage.

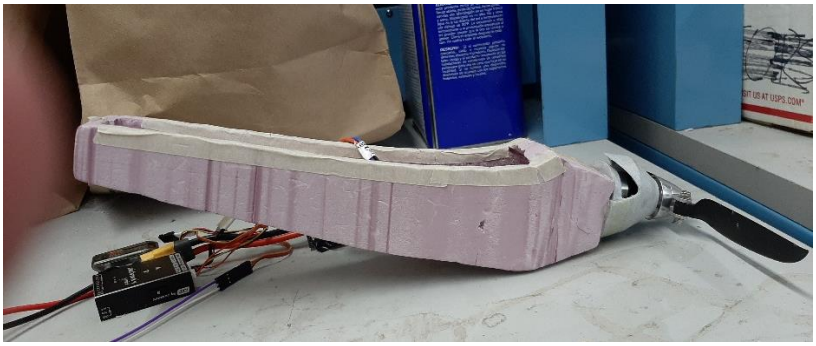

Figure 53. Final Fuselage Side-View

5.2.3 Control Surfaces

The control surfaces were cut from the wing using the foam cutter once the glue had fully set. The leading edges were rounded off using sandpaper to avoid interference during rotation. Meanwhile, a 1/16" thick rectangular piece of balsa wood was glued onto the underside of the central trailing section of the wing between the elevons. Foam was removed from the rear of the wing to make room for the servos, which were then glued down in the space. Balsa wood supports were required for stiffness. Servo arms were glued to the elevons and inserted into the servos.

The final modification involved the addition of a supporting control rod to the elevons. A small hole was drilled approximately 4cm into the outer edge of each elevon along the axis of rotation. The control rod was inserted into the elevon and a 90-degree bend allowed the opposite end of the rod to be glued into place as shown in Figure 54.

Figure 54. Supporting Control Rod

6 TESTING AND ANALYSIS

The flight characteristics of the MAV, including stability, control surface effectiveness, and gliding capability were evaluated through a series of basic flight tests. These included tethered lasso tests, unpowered glide tests, and a powered flight test. We also conducted a simple bend test to verify the strength of our chosen polystyrene foam, *Foamular 1000.*

6.1 Lasso Tests

The lasso tests consisted of attaching a string to the fuselage at the center of gravity. One team member held the string and proceeded to circle the aircraft in a lasso-type motion. This method minimizes the risk of damage to their aircraft. Figure 55 shows a team member conducting a typical lasso test.

Figure 55. Still from Lasso Test

The goal of this test was to observe the aircraft's yaw, pitch, and roll behavior. Anomalies involving the Pixhawk 4 mini prevented the team from obtaining useful flight data from these tests.

From the lasso test, the MAV's static stability, as well as the effectiveness of the control surfaces, was verified.

6.2 Glide Tests

Glide tests were conducted to observe the MAV's untethered flight behavior. As with the lasso tests, the team wanted to analyze the yaw, pitch, and roll behavior of the MAV. Figure 56 shows the method for hand launching the MAV. Thought data could not be extracted from the Pixhawk, video recordings of the tests revealed areas of improvement. The footage revealed the aircraft's tendency to roll immediately after release, which could not be corrected quick enough by the pilot. Such tendencies were fixed by trimming the elevons. Frequent collisions with ground during the glide tests served as validation of their MAV's durability.

Figure 56. Still from Glide Test

6.3 Powered Flight Test

The final test conducted was the powered flight test which the team was able to do with the help of a pilot, Jack Tulloch. Figure 57 is a still from the footage that was recorded of the test, the MAV can be seen near the top center.

Figure 57. Still from Powered Flight Test

The pilot suggested that the aircraft was tail-heavy, evidenced by the aircraft's tendency to pitch up. Additionally, the aircraft displayed a tendency to roll excessively. After this flight, the pilot suggested increasing the size of the MAV's vertical stabilizer further.

7 COMPETITION REVIEW

The competition between the two WPI teams will take place virtually with each team expecting to submit their results by April 16th, 10 days after the project deadline. As such, there are no competition results to report currently.

8 SUMMARY, CONCLUSIONS, RECOMMENDATIONS, BROADER IMPACTS

The purpose of the 2021 MAV Major Qualifying Project was to design and build a Micro Aerial Vehicle capable of carrying a payload, flying for a specified amount of time, and taking inertial measurements during flight. The final MAV was created through an iterative process over three academic terms; each iteration was improved based on results from testing the previous model.

This MQP report concludes with a recap of what was accomplished throughout development of the aircraft. The first term of the project focused on gathering information on existing MAVs and other aircraft to effectively create possible designs which would satisfy the design requirements. In the second term, detailed analyses on the selected wing, fuselage, weight distribution and other considerations were conducted as well as some preliminary construction and manufacturing. Most of manufacturing and testing occurred in the third term to create the final design. A competition between the two MQP teams will take place after the submission of this report.

At the submission of this report, the team had been unable to meet the objectives laid out by the competition goals. Minor issues remained related to the stability of our aircraft, which the team believed could be fixed by the April 16th competition deadline.

8.1 Recommendations for Future Work

After the conclusion of this project, the team has reflected on their experiences throughout the process that culminated in the final MAV. It is important to note that most of the team's efforts were done remotely due to the novel COVID-19 pandemic.

For future projects, we recommend taking theoretical designs to the laboratory for testing sooner rather than later. Laboratory testing will reveal problems that theory and simulations will not. For example, manufacturing the MAV was incredibly difficult to perfect on the first try. Had the team known which methods would be more effective through laboratory testing, the time spent researching manufacturing techniques may have been reduced.

The team also recommends acknowledging the impact that building a larger aircraft has on the ease of manufacturability. Because the team's aircraft was so small, the issue of fitting all the components inside the fuselage came up. The team's solution was to increase the size of the aircraft at the cost of score.

As built, the aircraft is fully capable of controlled flight. However, the next step would be to implement autonomous flight. Due to time constraints, the team was unable to attempt autonomy as it would have greatly increased the scope of this project.

8.2 Project Broader Impacts

The inexpensive construction of the aircraft combined with the ability to carry an interchangeable payload allows the aircraft to be configured for autonomous delivery. An autonomous MAV of this size could be used for short range delivery of small items such as medicine. It can be dangerous for the elderly population to go to the store to pick up their medications. With a form of autonomous delivery, this population will not have to risk their lives to simply continue living.

Also, the team's aircraft could be easily adapted into mass manufacturable kit and marketed as a retail toy for children interested in STEM. This toy could help inspire another generation to become aerospace engineers and solve the aeronautical problems of tomorrow.

9 REFERENCES

Administration, F. A. (2016). Flight Controls. In *Pilot's Handbook of Aeronautical Knowledge* (FAA-H-8083-25B ed., pp. 1-12): United States Department of Transportation, Federal Aviation Administration, Airman Testing Standards Branch.

ANSYS fluent 12.0 Theory Guide. (2009). Retrieved from https://www.afs.enea.it/project/neptunius/docs/fluent/html/th/main_pre.htm

Carter, B. D., Mayo, D. L.-J., & Godlewsk, N. A. *Design of a micro aerial vehicle.* Retrieved from WPI

Combustible, A. (2017). Polystyrene Panels: Should You Choose Expanded or Extruded Polystyrene. Retrieved from https://www.usimm.ca/en/polystyrene-panels-should-you-choose-expanded-or-extruded-polystyrene/

Corning, O. (2011). FOAMULAR® Extruded Polystyrene (XPS) Insulation Types and Physical Properties. In F. D. Sheet (Ed.): Owens Corning Foam Insulation.

Drela M. (1989) XFOIL: An Analysis and Design System for Low Reynolds Number Airfoils. In: Mueller T.J. (eds) Low Reynolds Number Aerodynamics. Lecture Notes in Engineering, vol. 54. Springer, Berlin, Heidelberg. https://doi.org/10.1007/978-3-642-84010-4_1

Eubanks, W. (2018). Rigid Foam Insulation. In T. o. Polystyrene (Ed.): Green and Growing.

Staples, G. (2014, April 12). Propeller Static & Dynamic Thrust. Retrieved February 02, 2021, from https://www.electricrcaircraftguy.com/2014/04/propeller-static-dynamic-thrust-equation-background.html

Grasmeyer, J. M. a. K., Matthew T. (2001). *Development of the Black Widow Micro Air Vehicle*. Retrieved from Simi Valley, CA:

Hassanalian, M., & Abdelkefi, A. (2017). Design, manufacturing, and flight testing of a fixed wing micro air vehicle with Zimmerman planform. *Meccanica, 52*(6), 1265-1282. doi:10.1007/s11012-016-0475-2

Hassanalian, M., Khaki, H., & Khosrawi, M. (2014). A new method for design of fixed wing micro air vehicle. *Institute of Mechanical Engineers: Journal of Aerospace Engineering*. doi:10.1177/0954410014540621

Henry, D. B., De Barros, I.-A. A., Wong, J., McWilliams, K. J., & Falcone, M. H. (2001). *Design of a micro aerial vehicle*. Retrieved from WPI

Jasak, H. (1996). *Error analysis and estimation for the finite volume method with applications to fluid flows*. Imperial College London (University of London).

Johnson, P. K. (2002). Balsa Wood. *Construction Materials.* Retrieved from https://airfieldmodels.com/information_source/construction_materials_for_model_building/balsa.htm

Kurtulus, D. F. (2011a). *Introduction to micro air vehicles: concepts, design, and applications*. Ankara, Turkey: Von Karman Institute for Fluid Dynamics.

Kurtulus, D. F. (2011b). Introduction to Micro Air Vehicles: Concepts, Design, and Applications. In *Recent developments in unmanned aircraft systems (UAS, including UAV and MAV)* (pp. 219 - 255). Ankara, Turkey: Von Karman Institute for Fluid Dynamics.

Manikanta Babu, N. (2016). *Controller based Electronic Speed Controller for MAV Propulsion System*.

Raymer, D. P. (2018). *Aircraft Design: A Conceptual Approach*. Reston, Virginia: American Institute of Aeronautics and Astronautics, Inc.

Shams, T., Shah, S., Javed, A., & Hamdani, S. (2020). Airfoil Selection Procedure, Wind Tunnel Experimentation, and Implementation of 6DOF Modeling on a Flying Wing Micro Aerial Vehicle. *Micromachines (Basel)*, *11*(6), 553–. https://doi.org/10.3390/mi11060553

Shiva Durga Madhav, G. S., Yelluri, & Govardhan, D. (2018). Design and Analysis of Micro Air Vehicle with Zimmerman Planform. In (Vol. Vol. 8, Issue 2). Hyderabad, India: International Journal of Mechanical and Production
Engineering Research and Development (IJMPERD).

Taylor, S. E. (2009). Biologically Inspired Wing Planform Optimization. In: Worcester Polytechnic Institute.

Wimbrow, J. M., Houghton, J. W., & Sartorelli, R. J. (2003). *Design of a radio-controlled micro air vehicle*. Retrieved from WPI

Winslow, J. (2018). Basic Understanding of Airfoil Characteristics at Low Reynolds Numbers (104 - 105). Journal of Aircraft, 55(3).

Winslow, J., Benedict, M., Hrishikeshavan, V., & Chopra, I. (2016). Design, development, and flight testing of a high endurance micro quadrotor helicopter. *International Journal of Micro Air Vehicles, 8*(3), 155-169. doi:10.1177/1756829316653694

Thipyopas, C. a. M., Jean-Marc. (2009). A Fixed-Wing Biplane MAV for Low Speed Missions. *1*(1).

Yechout, T. R., Morris, S. L., Bossert, D. E., Hallgren, W. F., & Hall, J. K. (2003). *Introduction to aircraft flight mechanics*. Reston, VA: American Institute of Aeronautics and Astronautics.

10 APPENDICES

Appendix 1: E-Flite Model Power Requirements

Determine a Model's Power Requirements:

1. Power can be measured in watts. For example: 1 horsepower = 746 watts
2. You determine watts by multiplying 'volts' times 'amps'. Example: 10 volts x 10 amps = 100 watts

Volts x Amps = Watts

3. You can determine the power requirements of a model based on the 'Input Watts Per Pound' guidelines found below, using the flying weight of the model (with battery):

- 50-70 watts per pound; Minimum level of power for decent performance, good for lightly loaded slow flyer and park flyer models
- 70-90 watts per pound; Trainer and slow flying scale models
- 90-110 watts per pound; Sport aerobatic and fast flying scale models
- 110-130 watts per pound; Advanced aerobatic and high-speed models
- 130-150 watts per pound; Lightly loaded 3D models and ducted fans
- 150-200+ watts per pound; Unlimited performance 3D models

NOTE: These guidelines were developed based upon the typical parameters of our E-flite motors. These guidelines may vary depending on other motors and factors such as efficiency and prop size.

4. Determine the Input Watts per Pound required to achieve the desired level of performance:

Model: Hangar 9 P-51 Miss America
Estimated Flying Weight w/Battery: 9.0 lbs
Desired Level of Performance: 90-110 (100 average) watts per pound; Fast flying scale model

9.0 lbs x 100 watts = 900 Input Watts per Pound of power (minimum) required to achieve the desired performance

5. Determine a suitable motor based on the model's power requirements. The tips below can help you determine the power capabilities of a particular motor and if it can provide the power your model requires for the desired level of performance:

- Most manufacturers will rate their motors for a range of cell counts, continuous current and maximum burst current.
- In most cases, the input power a motor is capable of handling can be determined by:

Average Voltage (depending on cell count) x Continuous Current = Continuous Input Watts

Average Voltage (depending on cell count) x Max Burst Current = Burst Input Watts

HINT: The typical average voltage under load of a Ni-Cd/Ni-MH cell is 1.0 volt. The typical average voltage under load of a Li-Po cell is 3.3 volts. This means the typical average voltage under load of a 10 cell Ni-MH pack is approximately 10 volts and a 3 cell Li-Po pack is approximately 9.9 volts. Due to variations in the performance of a given battery, the average voltage under load may be higher or lower. These however are good starting points for initial calculations.

Model: Hangar 9 Miss America
Estimated Flying Weight w/Battery: 9.0 lbs
Input Watts Per Pound Required for Desired Performance: 900 (minimum)

Motor: Power 60
Max Continuous Current: 40A*
Max Burst Current: 60A*
Max Cells (Li-Po): 5-7

6 Cells, Continuous Power Capability: 19.8 Volts (6 x 3.3) x 40 Amps = 792 Watts
6 Cells, Max Burst Power Capability: 19.8 Volts (6 x 3.3) x 60 Amps = 1188 Watts

Per this example, the Power 60 motor (when using a 6S Li-Po pack) can handle up to 1188 watts of input power, readily capable of powering the P-51 Miss America with the desired level of performance (requiring 900 watts minimum). You must however be sure that the battery chosen for power can adequately supply the current requirements of the system for the required performance. You must also use proper throttle management and provide adequate cooling for the motor, ESC and battery.

Appendix 2: WPI Internal Competition Rules

1. Mission Requirements

The competition design goal is to fly the smallest aircraft to take-off from a specified take-off/landing area, carry a specified payload for a minimum of two minutes, return, and land in the take-off/landing area. The aircraft's ability to perform this mission will be scored based on the aircraft's time of flight (endurance), longest straight-line distance that can be measured on the aircraft **(**more details later**),** and the number of independent inertial measurements that are successfully achieved.

Competing designs are limited to fixed wing aircraft only. All parts of the aircraft must be purchased through WPI-provided funds for the MQP. Students' personal funds may not be used to purchase any hardware or software parts of the aircraft.

1.1 Competition Venue

Competition venue details will be developed during the project based on circumstances as the academic year proceeds.

1.2 Payload

Payload will be in the form of one standard medicine pill bottle filled with sand provided to the students.

The payload will be filled with sand to weigh 55 grams total. Any empty space in the pill bottle may be packed with tissue to keep the sand from shifting during flight

Students may not modify the payload. The payload will be weighed just prior to all qualifying and competition flights.

1.3 General Airfield Layout

The general airfield layout is shown in the following figure.

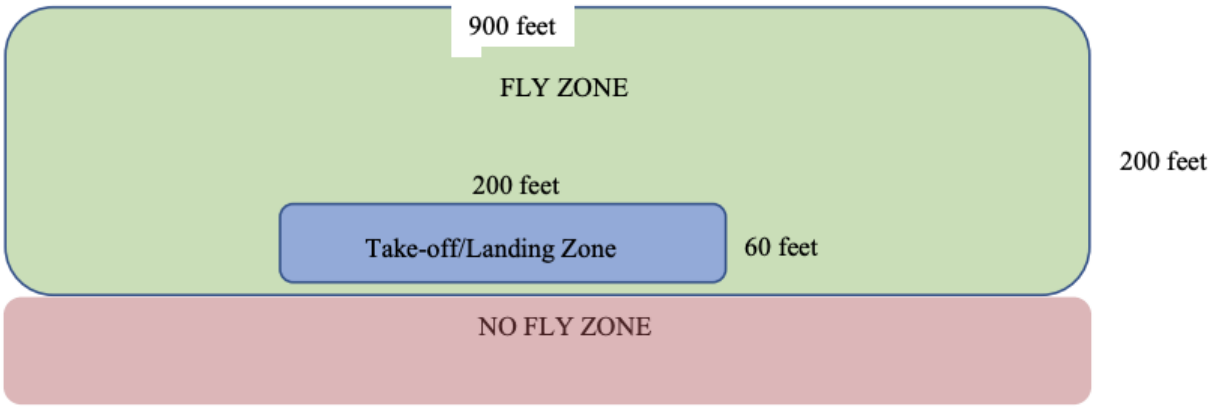

Plan of Airfield

1.4 Fly Zones

- Specific no-fly zones will be defined for the competition venue (see figure above)
- At no time will an aircraft enter the no-fly zones, whether under controlled flight or uncontrolled.
- At no time will an aircraft's altitude exceed 100 m above ground level.
- First infraction for crossing into the no-fly zone will result in an invalidated flight attempt and zero points will be awarded for that flight.
- Second infraction will result in disqualification from the entire event and loss of all points.
- It is the team and team pilot's responsibility to be aware of the venue-specific no-fly zones and to comply with all venue specific rules.
- If a team is unable to directionally control their aircraft and it is headed towards or is in a no-fly zone, the judges may order the pilot to intentionally crash the aircraft to prevent it from endangering people or property. This safety directive must be followed immediately if so ordered.

1.5 Take-off

Allowable methods of take-off include hand launch, ground roll, and catapult launch. The take-off method should account for the possibility of snow cover on the ground. The aircraft must climb to an observable ground clearance (see Section 1.6) by the end of the take-off zone. An aircraft that 'touches down' within the take-off zone after initial launch but still attains this observable take-off ground clearance completes a successful take-off.

1.6 Flight

The aircraft must fly at an observable ground clearance (distance between lowest point on aircraft including external payload and the ground) throughout the flight between take-off and landing. A judge using normal vision standing in the take-off/landing zone must be able to observe this ground clearance OR the team must independently provide clear evidence that this rule is met within 10 minutes after the completion of the flight. A flight will be considered as immediately terminated for scoring purposes the first time this rule is violated outside the take-off/landing zone.

1.7 Landing

- The take-off/landing zone will be visibly marked.
- It is the team and team pilot's responsibility to be aware of the class specific landing zone dimensions at the event site.
- All aircraft must remain within the designated landing zone runway during landing. Any aircraft that leaves their designated landing zone during landing are subject to a penalty of 50% of any points earned during the flight prior to landing.
- Any flight where the aircraft does not make the initial touch down for landing inside the designated landing zone is disqualified and forfeits all points for that flight.
- Any landing where the aircraft is not rolling or sliding on the ground when it leaves the landing zone (i.e., bouncing into the air as it leaves the landing zone) is disqualified. Touch-and-go landings are not allowed and will be judged as a failed landing attempt.
- The criteria for being within the landing zone is that no supporting part of the aircraft that is touching the ground can be outside the landing zone. For example, a wing tip or fuselage is

allowed to overhang the edge of the landing zone, as long as no supporting part of the aircraft is physically touching anything outside the landing zone.

1.8 Inertial Measurements

- **Successful inertial measurements** recorded from an onboard inertial measurement and/or GPS unit comprise a portion of the flight score. The following quantities may be measured to be included in the flight score: body-axis angular orientations (pitch, roll, yaw), angular velocities in pitch, roll and yaw, aircraft x-y position, aircraft altitude, aircraft velocity.

  To count as a valid measurement, quantity must be measured vs time for a 30 second duration, and graph of quantity vs time must be presented to competition judge within 20 minutes after end of flight. ***To demonstrate inertial measurements, the pill bottle payload may be replaced by the inertial measurement system during a competition flight.***

1.9 On the Day of the Competition

No changes to aircraft except ballast adjustments and replacement of batteries and/or propellers will be allowed after reaching the competition venue on the day of the competition.

The faculty advisors on the MAV MQP projects will serve as judges during the flight competition and to interpret competition rules throughout the MQP projects.

2 Design Constraints

2.1 Empty CG

All aircraft must meet the following Center of Gravity (CG) related requirements:

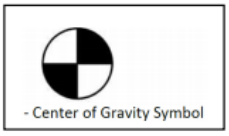
- Center of Gravity Symbol

- All aircraft must be flyable at their designated Empty CG position (no payload, ready to fly).
- All aircraft must have the fuselage clearly marked on both sides with a classic CG symbol (below) that is a minimum of 0.5 inches in diameter centered at the Empty CG position (Wing type aircraft may place the two CG markings on the bottom of the wing.)

2.2 Gross Weight Limit

There is no gross weight limit for aircraft, but aircraft weight will be naturally limited by scoring equation.

2.3 Controllability

All aircraft must be remotely controllable at all times during flight.

2.4 Radio Control System

The use of a 2.4 GHz radio control system is required for all aircraft. The 2.4 GHz radio control system must have a functional fail-safe system that will reduce the throttle to zero if the radio signal is lost.

2.5 Spinners or Safety Nuts Required

All powered aircraft must utilize either a spinner or a rounded model aircraft type safety nut.

2.6 Metal Propellers

Metal propellers are not allowed.

2.7 Lead is Prohibited

The use of lead in any portion of any aircraft (payload included) is strictly prohibited.

2.8 Payload Distribution

The payload cannot contribute to the structural integrity of the airframe.

2.9 Aircraft Ballast

Aircraft ballast, defined as non-payload weight needed to alter CG location, is allowed with the following conditions:

- Ballast cannot be used in a closed payload bay
- Ballast locations must be clearly indicated on the 2D drawings in MQP report.
- Ballast must be secured so as to avoid shifting or falling off the aircraft, thereby shifting the CG.
- Ballast will not be counted as payload.

2.10 Stored Energy Restriction

Aircraft must be powered by electric motors on board the aircraft. No other internal forms of stored potential energy allowed on the aircraft. Stored potential or elastic energy is allowed in a catapult launch mechanism.

2.11 Control Surface Slop

Aircraft control surfaces and linkage must not feature excessive slop. Sloppy control surfaces lead to reduced controllability in mild cases, or control surface flutter in severe cases.

2.12 Servo Sizing

Analysis and/or testing must be described in the Design Report that demonstrates the servos are adequately sized to handle the expected aerodynamic loads during flight.

2.13 Clevis Keepers

All control clevises must have additional mechanical keepers to prevent accidental opening of the control clevis in flight.

2.14 Red Arming Plug

All electric powered aircraft must use a discrete and removable red arming plug to arm and disarm the aircraft propulsion system. This red arming plug must be integrated into the electrical circuit between the battery and the electronic speed controller (ESC).

- The red arming plug must physically be located at 40% to 60% of the aircraft length from the aircraft propeller. This is to allow arming and disarming the aircraft at a safe distance from the propeller.
- The red arming plug must be located on top of the fuselage or wing and external of the aircraft surface.
- The location of the red arming plug must be clearly visible.
- The non-removable portion of the arming plug interface may not have more than one male lead.
- Disconnecting wiring harnesses to arm and disarm a system will **not** be allowed.

2.15 Battery Protection

- All batteries in the aircraft must be positively secured so that they cannot move under normal flight loads.
- The battery bay or location in the aircraft must be free of any hardware or other protrusions that could penetrate the battery in the event of a crash.

2.16 Power Limiter

All aircraft must use a 750 W power limiter such as in this link

https://neumotors.cartloom.com/storefront/product/24377. Note: You cannot purchase limiter at this link which was for an old SAE competition.

2.17 Aircraft Systems Requirements

- Propulsion requirements: aircraft are restricted to electric motor propulsion only.
- Propeller and gearbox: gearboxes on an aircraft where the propeller RPM differs from the motor RPM are allowed. Multiple motors, multiple propellers, propeller shrouds, and ducted fans are allowed.
- *The aircraft should use Lithium Polymer batteries. The maximum size propulsion system battery allowed is a 3-cell 1000 mAh lithium polymer battery. Batteries having fewer cells and lower capacity are permitted.*
- Gyroscopic assist and other forms of stability augmentation are allowed.
- Aircraft empty weight definition: All aircraft parts that are not payload contribute to the empty aircraft weight, including, but not limited to: airframe, receiver, electronics, batteries, hardware, brackets, straps and other associated features.

3 Scoring Metric

To receive a score on the day of the competition, teams must demonstrate the following flight sequence: take-off, complete range leg (flight time t_{flight} from take-off to drop used in scoring equation), drop payload, return and land. The flight score S is given by the following equation. The highest flight score among at most three attempts on the day of the competition will be considered.

$$S = 5\frac{T}{L^2} + 0.1875\sum_n A_n$$

The parameter T is related to t = time of flight (endurance) by;

For t < 120 secs	T = 0
For 120 < t < 240 secs	T = t
For t > 240 secs	T = 240

The parameter L (in cm) is the largest straight-line distance that can be measured on the aircraft. An L measurement stand, which consists of two vertical rods that move along a linear scale , will be provided. The distance between the vertical rods will be reduced until the aircraft no longer fits between the rods to measure L.

A_n = Points for demonstrating inertial measurements, one point each for 9 possible measurements (see Section 1.8). $A_1 = 1$ if pitch angle measured, $A_2 = 1$ if roll angle measured, etc.

4 Operational Safety Requirements

4.1 Ground Safety and Flight Line Safety Equipment

- No open toe shoes allowed. All team participants, including faculty advisors and pilots, will be required to wear closed-toe shoes during flight testing and during flight competition.
- All students involved at the flight line launching aircraft must wear safety glasses and hard hats.
- The University name must be clearly displayed on the wings or fuselage.
- The University initials may be substituted in lieu of the University name provided the initials are unique and recognizable.

4.2 Team Pilots

All pilots must be current members of the Academy of Model Aeronautics or the Model Aircraft Association of Canada (AMA has an agreement with MAAC).

A current WPI student who meets this requirement is available to MQP teams. If an MQP student on a team is an experienced RC pilot and AMA member, they can serve as the pilot. However, MQP teams should not plan on training an inexperienced student.

4.3 Aircraft Configuration during Flight

The aircraft must remain intact during a flight attempt to receive full flight score. A flight attempt includes activities at the starting line, the take-off roll, takeoff, flight, landing and recovery after landing.

A 25% deduction from the flight score will be assessed if any of the following items are observed to completely detach from the aircraft during a flight attempt.

- Stickers
- Tape
- Coverings

With the exception of a broken prop during landing, if any other components fall off the during a flight attempt, the flight will be disqualified.

5 Reporting Requirements

5.1 2D Drawing Requirements

*Updated 2D drawings should be provided by each team to faculty advisors periodically throughout the project **and** in all draft MQP report submissions.*

5.2 2D Format and Size

The 2D drawing must be ANSI B sized page (PDF) format (11 x 17 inches). The drawing shall consist of one (1) page.

5.3 Views Required

Drawings shall include at a minimum, a standard aeronautical 3-view orthographic projection arranged as described:

- Left side view, in lower left, with nose pointed left.
- Top view, above and aligned with the left side view, also with nose pointed left (wing-span break-view permitted).
- Front view aligned to side view, located in the lower right (projection view nonstandard movement as noted by projection view arrows in accordance with ANSIY14.5M 1994).

5.4 Dimensions Required

Drawing dimensions and tolerance shall be in SI units, decimal notation accordance with ANSI-Y14.5M 1994 to an appropriate level of precision to account for construction tolerances (allowable variation from analyzed prediction to account for fabrication) (i.e. X.X = ± .1 cm; X.XX = ± .03 cm; X.XXX = ± .010 cm). The minimum required dimensions/tolerances are: Aircraft length, width, and height.

5.5 Summary Data Required

The drawing shall contain a summary table of pertinent data to include but not limited to:

- Wingspan
- Empty weight
- Battery(s) capacity
- Motor make and model
- Motor KV (micro and Regular Class only)
- Propeller manufacturer, diameter, and pitch
- Servo manufacturer, model number and torque specification in ounce-inches for each servo used on the aircraft. Identify servo being used at each position on the aircraft.

5.6 Weight and Balance Information

The 2D drawing shall contain the following weight, balance and stability information:

- A clearly marked and labeled aircraft datum.
- A weight and balance table containing pertinent aircraft equipment. Each item listed must show its location from the aircraft datum in centimeters (the moment arm), the force, and resultant moment. The minimum list of pertinent equipment includes:
    - Motor
    - Battery(s)
    - Payload
    - Ballast (if used)
    - Electronics
- Design maximum payload, and design payload for maximum range
- Aircraft mean aerodynamic chord, stability margin and CG information listed below must be clearly shown on drawing:
    - Aircraft mean aerodynamic chord

- Stability margin for loaded CG and empty CG
- Empty CG location (flightworthy)
- Fully loaded CG (flightworthy, with payload, if applicable)

5.7 Tech Data Sheet: Weight Buildup

Updated Weight Buildup List should be provided by each team to faculty advisors periodically throughout the project **and** in all draft MQP report submission.

The Weight & Balance Build-up List will help teams understand the importance of managing aircraft weight to achieve safety of flight at the desired payload fraction. Each team shall supply a one (1) sheet summary list of aircraft parts, part weight, and part weight percentage) that contribute to the overall empty weight of the aircraft.

5.8 Flight Tests

The following flight tests are required;

1. An unpowered glide flight test is required for the B-term MQP report.

2. Take-off and landing (as described in Sections 1.5 and 1.6) and at least **one minute** of flight time with an empty (no payload) aircraft prior to the final competition date.

Appendix 3: WPI MAV Virtual Competition Rules

2021 WPI MAV VIRTUAL COMPETITION

- This year's competition is 'virtual' where MQP teams videotape their MAV flights to be submitted by Friday, April 16, 2021 at 7 pm. At a later time, faculty advisors will view and judge the final videos that teams submit to determine a team's final competition score.

- It is suggested that MAV flights be conducted on WPI football field with Institute Park as a backup. Teams must inform campus police of intended flights on WPI football field. Faculty advisors do not need to be present at the flights. You may videotape qualifying flights, scoring flights and L measurement on different days, and also attempt to complete the flight requirements at multiple times. However, you should only submit one (your best) video for each requirement.

- In the submitted videos; teams should show as many of the following items as possible;

  -Qualifying flight with no pill bottle payload; See *Note 1* below

  -Scoring flight (for time of flight score) carrying payload; See *Note 1* below:

  -Scoring flight (for inertial measurements); please see *Note 2* below for more details on inertial measurement requirements.

  - Measurement of maximum distance *L* on MAV. This video may be recorded at a different time than flights. Prof. Jayachandran will provide measurement tools.

- Teams should submit a single PowerPoint file that includes links to playable videos.

  - Please use slide titles, etc. to make clear which video is being shown.

  - Teams should also include a summary slide in PowerPoint file that includes;

    1) A list of videos (from 3rd bullet above) that have been submitted.

    2) A summary of values for;

    -Time of flight T for scoring flight;
    -The measured maximum length L value for the MAV;
    -The number (up to 9) and list of inertial measurements that were successfully recorded.
    - Your team's calculated score S using

$$S = 17.4 * \frac{130.6 * T}{L^3} + 0.1875 \sum_n A_n$$

    -Faculty advisors will view videos to confirm these values.

- Teams may submit zipped folders or provide a master link to a shared site as needed, but make sure that your submission is 'plug and play', e.g. everything in PowerPoint file and videos can be viewed easily by advisors.

Note 1:

New guidance for virtual competition:

- Qualifying flight; A flight of least **one minute** of flight time with an empty (no payload) aircraft (From 2021 competition rules, Section 5.8).

- Scoring flight: A flight with pill bottle payload weighing 55 grams that flies for up to four minutes.

- For qualifying and scoring flights, the MAVs should be flown in an oval pattern consisting of multiple circuits within the confines of the selected flight site. The general airfield layout on page 1 of the 2021 WPI MAV competition rules will not be used. For safety, MAVs should not be flow near any persons present at the test site at any time.

Note 2:

(from 2021 competition rules)

1.1 Inertial Measurements

- Successful inertial measurements recorded from an onboard inertial measurement and/or GPS unit comprise a portion of the flight score. The following quantities may be measured to be included in the flight score: body-axis angular orientations (pitch, roll, yaw), angular velocities in pitch, roll and yaw, aircraft x-y position, aircraft altitude, aircraft velocity.

  To count as a valid measurement, quantity must be measured vs time for a 30 second duration, and graph of quantity vs time must be presented to competition judge within 20 minutes after end of flight. ***To demonstrate inertial measurements, the pill bottle payload may be replaced by the inertial measurement system during a competition flight.***

New guidance for virtual competition (inertial measurements)

- In the inertial measurement video, teams must show that the final quantity vs time plots were obtained within 20 minutes after the MAV flight. Use a recorded iPhone timer, or time at bottom of video on playback bar (also called scrub bar, seek bar, progress bar). Teams should also *submit a single file showing all of their final quantity vs time plots* along with the PowerPoint slides and videos. Present high-quality plots with detailed and clear axis labels. Faculty advisors should <u>not</u> have to run any post-processing code to view the plots.

Appendix 4: Airfoil Performance Scores

Airfoil	Score (Highest to Lowest, Average of Eq. 15 & Eq. 16)
Selig 2046	8.5904
Selig 2027	8.2876
Eppler 328	8.0352
Selig 3010	7.9225
Clark Y	7.9221
Selig 4053	7.8803
Eppler 201	7.8334
Eppler 211	7.8018
Eppler 195	7.7944
Eppler 332	7.7757
Selig 9037	7.7716
Selig 7055	7.7419
Selig 2091	7.7155
GOE 796	7.7016
Eppler 205	7.6941
GOE 693	7.5558
Eppler 222	7.5409
Selig 7038	7.4311
Eppler 193	7.3845
Eppler 392	7.3337
Selig 5020	7.3079
Eppler 395	7.2949
Eppler 333	7.2413
GOE 623	7.1521
Davis	7.1142
Selig 3025	7.0718

Selig 4310	7.0264
Eppler 64	6.9702
Eppler 387	6.8929
Eppler 176	6.8927
Eppler 214	6.8370
N-10	6.8356
Eppler 174	6.7670
Selig 4022	6.3236
Eppler 678	6.3179
GOE 117	6.2139
GOE 285	5.9015
GOE 280	5.3173
GOE 178	5.2271
GOE 167	5.1971